

¹ **Nucleotide inhibition of the**

² **pancreatic ATP-sensitive K⁺ channel**

³ **explored with patch-clamp**

⁴ **fluorometry**

⁵ **Samuel G. Usher¹, Frances M. Ashcroft^{1*}, Michael C. Puljung^{1*}**

*For correspondence:

frances.ashcroft@dpag.ox.ac.uk

⁶ Department of Physiology, Anatomy and Genetics, University of Oxford,
(FMA);

michael.puljung@dpag.ox.ac.uk

(MCP)

⁷ Oxford OX1 3PT, United Kingdom

⁸

⁹ **Abstract** Pancreatic ATP-sensitive K⁺ channels (K_{ATP}) comprise four inward rectifier
¹⁰ subunits (Kir6.2), each associated with a sulphonylurea receptor (SUR1). ATP/ADP
¹¹ binding to Kir6.2 shuts K_{ATP}. Mg-nucleotide binding to SUR1 stimulates K_{ATP}. In the
¹² absence of Mg²⁺, SUR1 increases the apparent affinity for nucleotide inhibition at Kir6.2
¹³ by an unknown mechanism. We simultaneously measured channel currents and
¹⁴ nucleotide binding to Kir6.2. Fits to combined data sets suggest that K_{ATP} closes with
¹⁵ only one nucleotide molecule bound. A Kir6.2 mutation (C166S) that increases channel
¹⁶ activity did not affect nucleotide binding, but greatly perturbed the ability of bound
¹⁷ nucleotide to inhibit K_{ATP}. Mutations at position K205 in SUR1 affected both nucleotide
¹⁸ affinity and the ability of bound nucleotide to inhibit K_{ATP}. This suggests a dual role for
¹⁹ SUR1 in K_{ATP} inhibition, both in directly contributing to nucleotide binding and in
²⁰ stabilising the nucleotide-bound closed state.

²¹

22 Introduction

23 ATP-sensitive K⁺ channels (K_{ATP}) couple the metabolic state of a cell to its electrical ac-
 24 tivity (*Ashcroft and Rorsman, 2013*). In pancreatic β-cells, closure of K_{ATP} in response to
 25 glucose uptake triggers insulin secretion. As such, mutations in K_{ATP} that affect its re-
 26 sponse to changes in cellular metabolism cause diseases of insulin secretion, e.g. neona-
 27 tal diabetes and persistent hyperinsulinemic hypoglycaemia of infancy (PHHI; *Quan et al.*
 28 (*2011*); *Ashcroft et al. (2017)*). K_{ATP} is composed of four inwardly rectifying K⁺ channel
 29 subunits (Kir6.2 in pancreatic β-cells), which form the channel pore and four modula-
 30 tory sulphonylurea receptor subunits (SUR1 in β-cells; Figure 1A; *Aguilar-Bryan et al.*
 31 (*1995*); *Inagaki et al. (1995)*; *Sakura et al. (1995)*; *Inagaki et al. (1997)*). SUR1 is a mem-
 32 ber of the ABC transporter family but lacks any transport activity (*Aguilar-Bryan et al.*,
 33 *1995*; *Tusnady et al., 1997*). K_{ATP} responds to metabolism via adenine nucleotide binding
 34 to three distinct classes of intracellular nucleotide-binding site (one on each Kir6.2 sub-
 35 unit and two on each SUR1 subunit—making twelve sites in total (*Vedovato et al., 2015*).
 36 Binding of ATP or ADP to Kir6.2 inhibits K_{ATP} channel activity (*Tucker et al., 1997*; *Proks*
 37 *et al., 2010*), whereas binding of nucleotides to SUR1 stimulates K_{ATP} (*Nichols et al., 1996*;
 38 *Tucker et al., 1997*). The stimulatory activity of nucleotides on K_{ATP} depends on Mg²⁺
 39 (*Gribble et al., 1998*), whereas their inhibitory effect on Kir6.2 does not (*Tucker et al.*,
 40 *1997*).

41 In addition to nucleotide-dependent activation, SUR1 confers several other properties
 42 on the Kir6.2. First, association with SUR1 increases the open probability (P_{open}) of Kir6.2
 43 (*Babenko and Bryan, 2003*; *Chan et al., 2003*; *Fang et al., 2006*). Despite this increase in
 44 P_{open} , SUR1 also paradoxically increases the apparent affinity for nucleotide inhibition at
 45 Kir6.2 by an unknown mechanism (*Tucker et al., 1997*). SUR1 is also responsible for high-
 46 affinity inhibition of K_{ATP} by antidiabetic sulphonylureas and glinides as well as activation
 47 by K_{ATP} -specific K⁺ channel openers (*Tucker et al., 1997*). Finally, SUR1 and Kir6.2 must co-
 48 assemble to ensure mutual exit from the endoplasmic reticulum and correct trafficking

⁴⁹ to the plasma membrane (*Zerangue et al., 1999*).

⁵⁰ To date, the primary means of studying nucleotide-dependent effects on K_{ATP} chan-
⁵¹ nel function has been with electrophysiological approaches, which measure the summed
⁵² activity of all three classes of binding site acting in concert. Thus, it can be difficult to sep-
⁵³ arate the contributions of each class of site to the opening and closing of the channel
⁵⁴ pore and to properly distinguish between nucleotide binding and channel gating. To
⁵⁵ overcome these limitations, we have applied a novel approach to directly measure nu-
⁵⁶ cleotide binding to each individual class of site in K_{ATP} (*Puljung et al., 2019*). This method
⁵⁷ utilizes Förster resonance energy transfer (FRET) between channels labelled with the flu-
⁵⁸ orescent unnatural amino acid 3-(6-acetylnaphthalen-2-ylamino)-2-aminopropanoic acid
⁵⁹ (ANAP) and fluorescent trinitrophenyl (TNP) analogues of adenine nucleotides (Figure 1B).
⁶⁰ As we show here, this method is readily combined with patch-clamp electrophysiology so
⁶¹ that nucleotide binding and regulation of current can be measured simultaneously. This
⁶² has enabled us to quantitatively assess nucleotide binding to Kir6.2 and explore how this
⁶³ is coupled to channel inhibition in both wild-type K_{ATP} and K_{ATP} carrying mutations that
⁶⁴ impair ATP inhibition.

⁶⁵ Results

⁶⁶ **Measuring nucleotide binding to Kir6.2.** We previously used this FRET-based bind-
⁶⁷ ing assay to measure nucleotide binding to the second nucleotide-binding site of SUR1
⁶⁸ (*Puljung et al., 2019*). To measure binding to Kir6.2 in the complete K_{ATP} complex (four
⁶⁹ full-length Kir6.2 subunits co-expressed with four full-length SUR1 subunits), we replaced
⁷⁰ a tryptophan at position 311 (W311) that is 26 Å from the location of the inhibitory nucleotide-
⁷¹ binding site on Kir6.2 with ANAP (Figure 1C) such that each subunit is labelled with one
⁷² ANAP molecule. We designate this construct Kir6.2*. Based on the theoretical FRET ef-
⁷³ ficiency calculated from the Förster equation and available cryo-EM structures (*Martin*
⁷⁴ *et al., 2017, 2019*), we expect 91% FRET efficiency between ANAP at position 311 and a
⁷⁵ TNP-ATP molecule bound to Kir6.2, and only 4% FRET efficiency to TNP-ATP bound to the

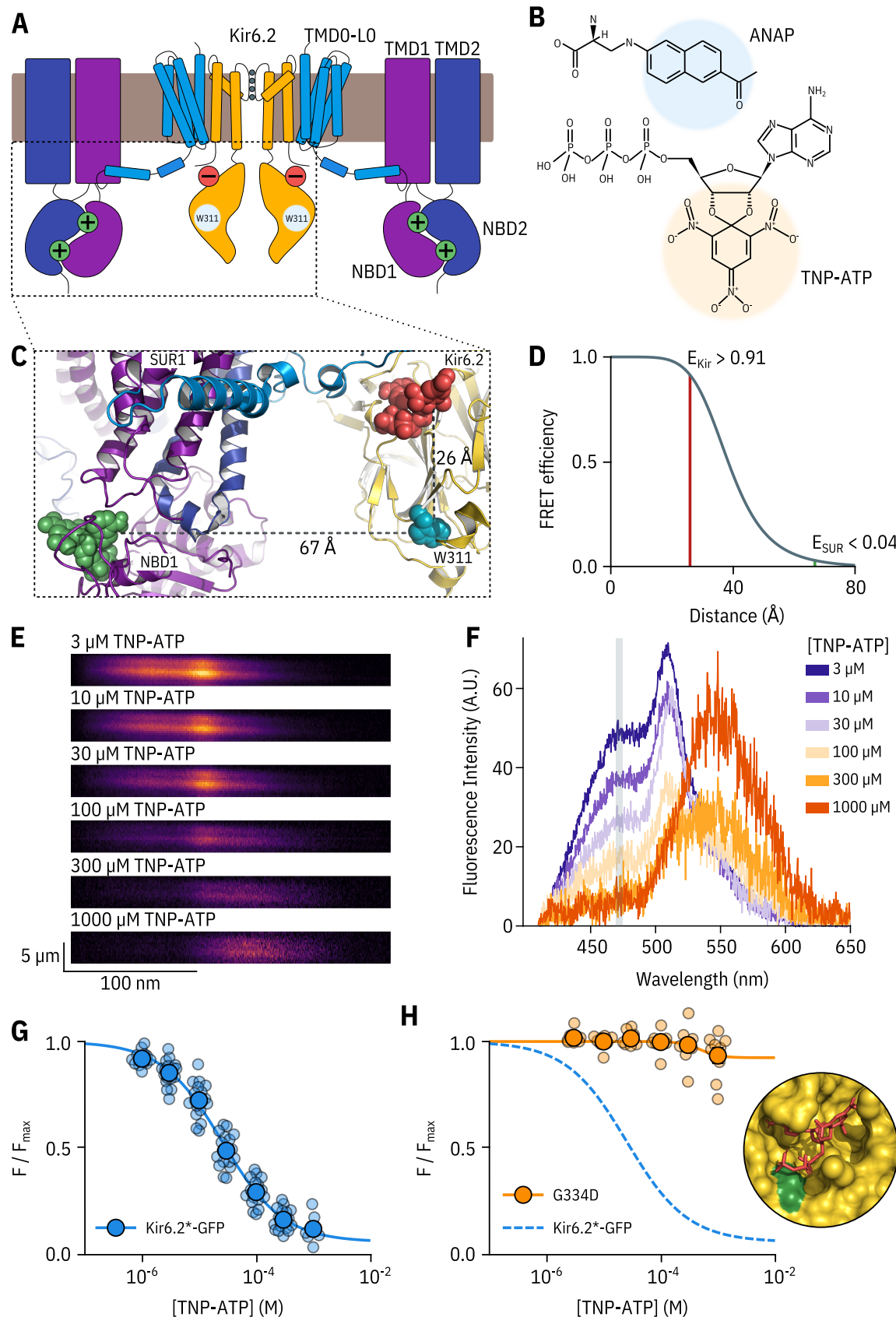


Figure 1. A FRET assay to measure nucleotide binding to Kir6.2.

Figure 1. A FRET assay to measure nucleotide binding to Kir6.2. **A.** Cartoon illustrating the topology of K_{ATP}. The inhibitory nucleotide-binding site on Kir6.2 is shown in red; the stimulatory nucleotide-binding sites on SUR1 are shown in green. The three transmembrane domains of SUR1 are designated TMD0, TMD1, and TMD2. The loop connecting TMD0 to TMD1 is designated L0. The nucleotide binding domains of SUR1 are labelled NBD1 and NBD2. **B.** Chemical structures of ANAP and TNP-ATP. The fluorescent moieties are highlighted. **C.** Side view of the structure of the cytosolic domains of Kir6.2 (PDB accession #6BAA) and one SUR1 subunit (PDB accession #6PZI). TNP-ATP (red, from PDB accession #5XW6) was docked into the nucleotide-binding site of Kir6.2 and positioned in NBS1 of SUR1 (green, from PDB accession #3AR7) by alignment as described in Materials and Methods. Distances from the native tryptophan at position 311 in Kir6.2 to the fluorescent moieties of the TNP-ATPs are displayed in Å. **D.** Theoretical FRET efficiency between ANAP and TNP-ATP as a function of distance, calculated from the Förster equation. The distances and corresponding FRET efficiencies between ANAP at position 311 and TNP-ATP bound to Kir6.2 (E_{Kir}) and SUR1 (E_{SUR}) are indicated. **E.** Spectral images acquired from an unroofed membrane expressing Kir6.2*-GFP + SUR1 and exposed to increasing concentrations of TNP-ATP. The y-dimension in each image represents distance. The x-dimension represents wavelength. **F.** Line-averaged, background-subtracted spectra from **E** displayed with increasing concentrations of TNP-ATP coloured from purple to orange. The three fluorophores have distinct peaks: ANAP at 472 nm, GFP at 508 nm, and TNP-ATP at 561 nm. The shaded rectangle indicates the wavelength range used to measure ANAP intensity. **G.** Concentration-response relationship for binding of TNP-ATP to Kir6.2*-GFP + SUR1 in unroofed membranes. Data were plotted as F/F_{max} , where F_{max} is the fluorescence intensity in the absence of nucleotide. The smooth curve is a descriptive Hill fit. $EC_{50} = 25.6 \mu M$, $h = 0.82$, $E_{max} = 0.93$, $n = 18$. **H.** Concentration-response relationship for binding of TNP-ATP to Kir6.2*-G334D-GFP + SUR1 in unroofed membranes. The dashed blue curve is the fit from **G**. The orange curve is a descriptive Hill fit to the G334D data. $EC_{50} = 493 \mu M$, $h = 2.63$, $E_{max} = 0.08$, $n = 9$. The inset shows the location of G334D (green) in relation to the inhibitory ATP binding site on Kir6.2 (PDB accession #6BAA). TNP-ATP (PDB accession #5XW6) shown in red sticks.

Figure 1 – figure supplement 1. ANAP labelling is specific and only full-length Kir6.2 is expressed at the cell membrane.

Figure 1 – figure supplement 2. Kir6.2*-GFP is functionally similar to Kir6.2-GFP.

⁷⁶ closest nucleotide-binding site on SUR1 (nucleotide binding site 1, Figure 1D). We also ex-
⁷⁷ pect very little FRET between ANAP at position 311 and TNP-ATP bound to neighbouring
⁷⁸ Kir6.2 subunits (15–25%).

⁷⁹ ANAP incorporation into Kir6.2 was achieved as described previously (*Chatterjee et al., 2013; Zagotta et al., 2016; Puljung et al., 2019*). Briefly, HEK-293T cells were co-transfected
⁸⁰ with a plasmid encoding a Kir6.2 construct with a C-terminal GFP tag and an amber stop
⁸¹ codon (TAG) replacing the codon corresponding to amino acid position 311 (W311^{TAG}-
⁸² GFP) and a plasmid encoding an ANAP-specific tRNA/tRNA synthetase pair (pANAP). We
⁸³ also included a dominant negative eukaryotic ribosomal release factor (eRF-E55D) in
⁸⁴ our transfections, which has been shown to increase the amount of full-length, ANAP-
⁸⁵ labelled protein (*Schmied et al., 2014; Puljung et al., 2019*). When cultured in the pres-
⁸⁶ ence of ANAP, full length, fully ANAP-labelled Kir6.2 protein was produced and success-
⁸⁷ fully trafficked to the membrane in the presence of SUR1 (Figure 1—Figure supplement 1;
⁸⁸ see Materials and Methods). ANAP fluorescence from labelled channels can be separated
⁸⁹ from unincorporated ANAP or autofluorescence based on emission spectra (*Puljung et al., 2019*).
⁹⁰ However, we found it much more convenient to first identify transfected cells or
⁹¹ membrane fragments based on the presence of a GFP tag. Thus, we used GFP-tagged
⁹² Kir6.2 constructs throughout this study, unless otherwise indicated.

⁹⁴ In all our experiments, we measured currents in excised patches from cells expressing
⁹⁵ K_{ATP} in the absence of Mg²⁺. Under such conditions, nucleotides can bind to both sites on
⁹⁶ SUR1, but no activation occurs, allowing inhibitory currents to be measured in isolation
⁹⁷ (*Gribble et al., 1998; Ueda et al., 1999; Puljung et al., 2019*). Kir6.2*-GFP + SUR1 exhib-
⁹⁸ ited nearly identical sensitivity to ATP inhibition as Kir6.2-GFP + SUR1 (Figure 1—Figure
⁹⁹ supplement 2A), indicating that replacement of W311 with ANAP did not affect inhibition
¹⁰⁰ by K_{ATP}. Both subunits also showed similar sensitivity to TNP-ATP, which inhibited with
¹⁰¹ a higher apparent affinity relative to ATP (Figure 1—Figure supplement 2B,C).

¹⁰² Kir6.2-GFP has been demonstrated to traffic to the plasma membrane in the absence
¹⁰³ of SUR1 (*John et al., 1998; Makhina and Nichols, 1998*). In a luminescence-based, surface-

104 expression assay, we did not detect HA-tagged Kir6.2*-GFP at the plasma membrane
 105 in the absence of SUR1 (Figure 1—Figure supplement 1E). To verify that the currents
 106 measured in our experiments in which Kir6.2*-GFP was co-transfected with SUR1 were
 107 the result of Kir6.2*-GFP + SUR1 and not Kir6.2*-GFP alone, we measured the sensitivity
 108 of currents to inhibition by the sulphonylurea tolbutamide, a property conferred by the
 109 SUR1 subunit. Whereas currents from unlabelled wild-type Kir6.2-GFP expressed in the
 110 absence of SUR1 were not affected by 100 μ M tolbutamide, both wild-type Kir6.2-GFP and
 111 Kir6.2*-GFP currents were inhibited to a similar extent by when expressed with SUR1
 112 (46.5% \pm 0.04% and 57.7% \pm 0.02%, respectively; Figure 1—Figure supplement 2D). The
 113 extent of block was similar to previous measurements of tolbutamide inhibition (*Tucker*
 114 *et al., 1997*), confirming that Kir6.2*-GFP was co-assembled with SUR1 at the plasma
 115 membrane.

116 To measure nucleotide binding, cells transfected with Kir6.2*-GFP + SUR1 were briefly
 117 sonicated, leaving behind unroofed plasma membrane fragments (*Heuser, 2000; Zagotta*
 118 *et al., 2016; Puljung et al., 2019*) containing ANAP-labelled K_{ATP} channels with the intra-
 119 cellular nucleotide-binding sites exposed to the bath solution. The sample was excited
 120 with a 385 nm LED and emitted fluorescence from the membrane fragments was passed
 121 through a spectrometer, allowing us to separate ANAP, GFP, and TNP-ATP fluorescence
 122 by peak wavelength (Figure 1E,F). As expected from FRET, increasing the concentration
 123 of TNP-ATP caused a decrement in the ANAP peak at 472 nm and a concomitant increase
 124 in the TNP-ATP peak at 561 nm (Figure 1F). We used the quenching of the ANAP peak
 125 as a direct measure of TNP-ATP binding as this signal was specific to K_{ATP} . In contrast,
 126 the peak TNP-ATP fluorescence may include contributions from both specific and non-
 127 specific nucleotide binding. Due to the sharp cut-off of the GFP emission spectrum at
 128 shorter wavelengths, our measurements of peak ANAP fluorescence were unaffected by
 129 the presence of the GFP tag on Kir6.2.

130 We fit concentration-response data for TNP-ATP quenching with the Hill equation, to
 131 produce estimates of apparent affinity and E_{max} (ANAP quenching at saturating concen-

trations of TNP-ATP; Figure 1G). E_{max} was 93%, in good agreement with the 91% predicted by the Förster equation and theoretical distance measurements (Figure 1D), suggesting that we were able to measure binding directly to the inhibitory site at Kir6.2. To confirm this, we introduced a well-studied neonatal diabetes mutation (G334D) into the Kir6.2 binding site, which drastically reduces the sensitivity of the channel to inhibition by nucleotides (**Drain et al., 1998; Masia et al., 2007; Proks et al., 2010**). Based on the cryo-electron microscopy structures of K_{ATP} , this mutation is expected to interfere with nucleotide binding directly (Figure 1H inset, **Martin et al. (2017)**). The resulting construct Kir6.2*,G334D-GFP + SUR1 displayed drastically reduced ANAP quenching over the range of TNP-ATP concentrations tested, with an E_{max} of 8%; again in good agreement with the predicted FRET efficiencies between ANAP at position 311 and TNP-ATP bound only to SUR1. We therefore conclude that our binding measurements were specific for the inhibitory nucleotide-binding site on Kir6.2. This observation is consistent with the interpretation that the G334D mutation causes neonatal diabetes by preventing nucleotide binding. However, the observed loss in nucleotide-dependent quenching in Kir6.2*-G334D-GFP may also be due to an allosteric effect of the G334D mutation on channel gating. We feel that this interpretation is unlikely, as G334D has been shown to have no effect on the unliganded P_{open} of K_{ATP} (**Proks et al., 2010**).

Measuring current inhibition and nucleotide binding simultaneously. The apparent affinity of Kir6.2*-GFP + SUR1 for TNP-ATP in unroofed membranes was 25.6 μM (Figure 1G and Table 1). This value is higher than the apparent affinity for nucleotide inhibition (6.2 μM) measured using patch-clamp (Figure 1—Figure supplement 2C). However, both binding and current measurement are a function of the intrinsic binding affinity, the channel P_{open} , and the ability of agonist, once bound, to close the channel. Furthermore, the functional state of K_{ATP} in unroofed membranes is unclear. This is a particular problem with K_{ATP} channels, which run down due to slow dissociation of phosphatidylinositol 4,5-bisphosphate (PIP₂), reducing the P_{open} over time even in the absence of nucleotides (**Proks et al., 2016**).

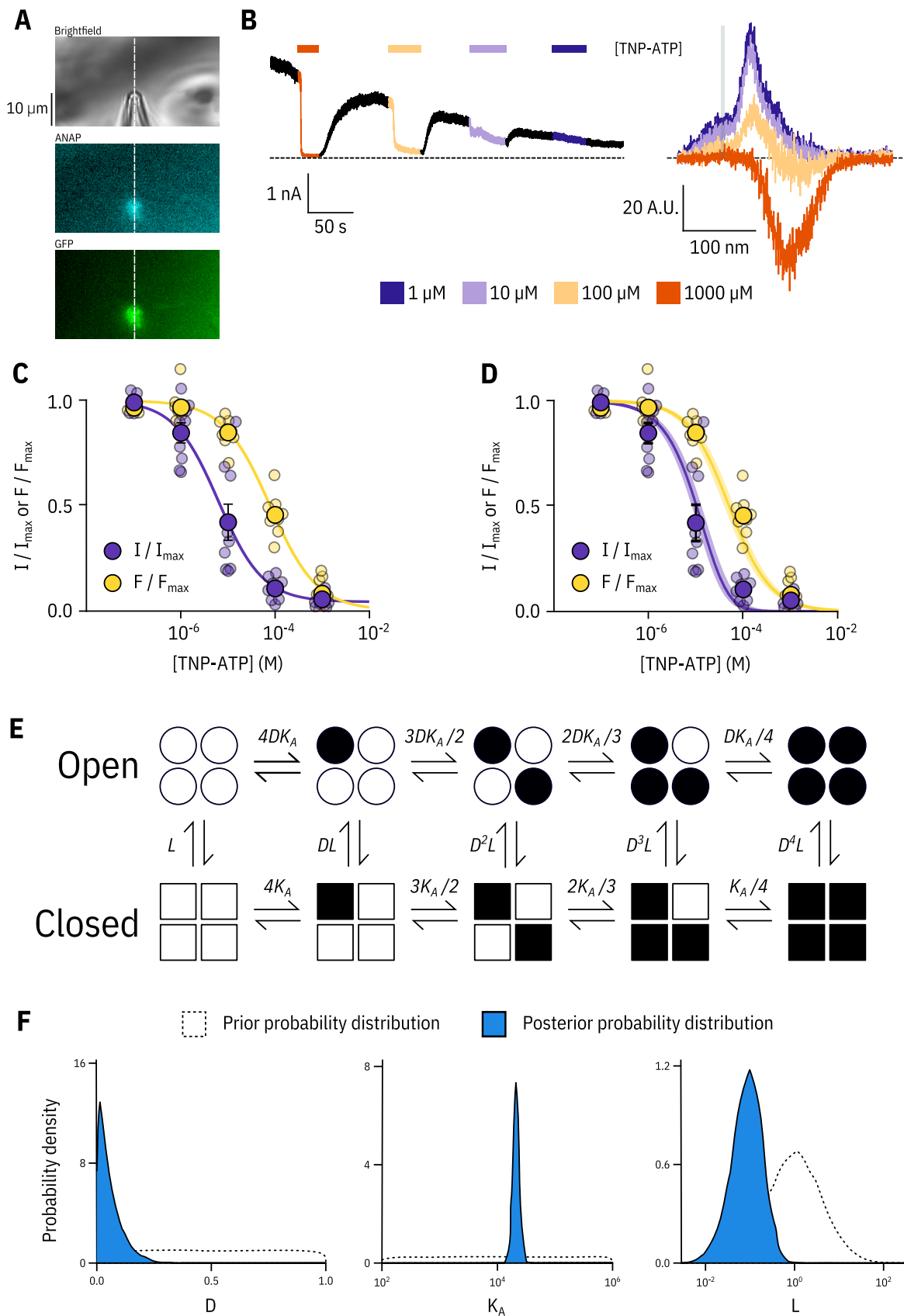


Figure 2. Simultaneous measurements of nucleotide binding and channel current.

Figure 2. Simultaneous measurements of nucleotide binding and channel current. **A.** Brightfield and fluorescence images of a patch pipette and excised, inside out patch expressing Kir6.2*-GFP + SUR1, with the location of the centre of the spectrometer slit overlaid as a white, vertical line. **B.** Current (left) and spectra (right) acquired from the same excised, inside-out patch exposed to TNP-ATP and coloured according to concentration. **C.** Concentration-response ($n = 9$) for TNP-ATP inhibition of Kir6.2*-GFP + SUR1 currents (I/I_{max}) and for quenching of ANAP fluorescence (F/F_{max}). Both current inhibition and fluorescence quenching were fit to the Hill equation. Current inhibition: $IC_{50} = 6.23 \mu\text{M}$, $h = 0.92$, $I_{max} = 0.96$, fluorescence quenching: $EC_{50} = 77.7 \mu\text{M}$, $h = 0.87$, $E_{max} = 1.00$. **D.** The same data as in **C** fit to an MWC-type model. Solid curves represent the median fit; shaded areas represent the 95% quantile interval. Values for the fits are reported in the text and in Table 3. **E.** MWC-type model for inhibition of K_{ATP} by nucleotides. Open subunits are shown as circles; closed are shown as squares. Nucleotide-bound subunits are represented by filled symbols. L , D , and K_A are defined in the text. **F.** Posterior probability distributions for the MWC-type model generated by MCMC fits to the data in **C** overlaid on the prior probability distribution (dashed line) for each parameter.

Figure 2 – figure supplement 1. Fixing L does not affect estimates of D and K_A .

Figure 2 – figure supplement 2. Model selection.

160 As measuring either nucleotide binding or ionic currents in isolation only offers lim-
 161 ited mechanistic insight into inhibition of K_{ATP} , we turned to patch-clamp fluorometry
 162 (PCF, *Proks et al. (2016); Zheng and Zagotta (2003)*). Using PCF, we can measure TNP-ATP
 163 binding to Kir6.2 and channel activity simultaneously (Figure 2), providing us with direct
 164 access to the relationship between nucleotide binding and channel function. We simu-
 165 taneously measured fluorescence emission spectra and ionic currents for Kir6.2*-GFP +
 166 SUR1 in inside-out, excised membrane patches. As before, all measurements were per-
 167 formed in the presence of Mg^{2+} chelators, such that nucleotide inhibition could be mea-
 168 sured in the absence of activation (*Tucker et al., 1997; Gribble et al., 1998*). Strikingly,
 169 current inhibition occurred at a lower range of concentrations compared to nucleotide
 170 binding (Figure 2C,D). The apparent EC_{50} for inhibition calculated from Hill fits was an or-
 171 der of magnitude lower than the EC_{50} for binding measured in the same patches (Figure
 172 2C, Table 2). We considered several different gating models to explain this observation.
 173 In each model, we assumed the channel pore was able to open and close in the absence

174 of ligand with an equilibrium constant L , where $P_{open} = L/(L + 1)$ and $L > 0$. This reflects
 175 the ability of K_{ATP} to open and close in the absence of nucleotides. Each model also
 176 had parameters representing the intrinsic binding affinity to the closed state (K_A , where
 177 $K_A > 0$) and the factor by which nucleotide binding favours channel closure (D , where
 178 $D < 1$).

179 Our simultaneous binding and current measurements were well fit with a Monod-
 180 Wyman-Changeux (MWC)-type model (Figure 2D,E; **Monod et al. (1965)**) which has been
 181 previously proposed to explain K_{ATP} channel inhibition (**Enkvetachakul and Nichols, 2003**;
 182 **Craig et al., 2008; Vedovato et al., 2015**). In our MWC-type model, each ligand binding
 183 event (K_A) is independent and each bound ligand favours the closed state by the same
 184 factor (D). Simultaneous measurement of binding (fluorescence) and gating (current) al-
 185 lowed us to obtain well constrained fits to our model. To obtain free parameter (L , K_A ,
 186 D) estimates and verify that each parameter was well and uniquely determined, we em-
 187 ployed a Bayesian Markov chain Monte Carlo (MCMC) method previously employed by
 188 Hines et al. (**Hines et al., 2014**). Using this approach, we constructed posterior proba-
 189 bility distributions for the free parameters of our MWC-type model (Figure 2F, Table 3).
 190 Based on these distributions, we estimated $K_A = 2.1 \times 10^4 \text{ M}^{-1}$ ($K_D = 47.9 \mu\text{M}$), $L = 0.09$
 191 ($P_{open} = 0.08$), and $D = 0.04$. The very low D value indicates that nucleotide binding was
 192 tightly coupled to channel closure; i.e. nucleotides have a very strong preference for the
 193 closed state of the channel. The low value for D also explains why the channels were
 194 nearly completely inhibited at TNP-ATP concentrations at which not all the binding sites
 195 were occupied, as well as the degree to which channel inhibition is complete at saturating
 196 concentrations of TNP-ATP. Our estimate of L was quite low and broadly distributed. We
 197 repeated our fits with L fixed to a value consistent with previous single channel measure-
 198 ments (0.8, $P_{open} = 0.45$, **John et al. (1998); Enkvetachakul et al. (2000); Ribale et al. (2006)**).
 199 This had only a very small effect on our estimates of D and K_A (Figure 2—Figure sup-
 200 plement 1). The broad distribution of L in our fit may represent current rundown which
 201 occurs during our patch-clamp recordings and is expected to affect the open-closed equi-

librium. Cross-correlation plots (in parameter space) of the values derived from our fits produced well bounded ellipsoids, indicating that our parameters were uniquely determined (Figure 2—Figure supplement 1A).

In addition to the full MWC-type model we considered alternate models (Figure 2—Figure supplement 2). These included a model in which only the first binding event influences the open-closed equilibrium of the channel (single-binding model; Figure 2—Figure supplement 2B, Table 3), and an MWC-style model with an additional parameter C to allow for direct negative cooperativity between binding sites (negative cooperativity model; Figure 2—Figure supplement 2C, Table 3). The single-binding model yielded very similar parameter estimates to our full MWC-type model (Figure 2—Figure supplement 2D, Table 3). This is a consequence of D being so low that even in the MWC-type model most channels are closed when only a single nucleotide is bound. The cooperative model improved our fits, but not enough to justify the inclusion of an additional free parameter (see Discussion).

Kir6.2-C166S affects the ability of bound nucleotides to close K_{ATP} . To provide a rigorous test as to whether our experimental system was capable of separating nucleotide binding from subsequent channel gating, we introduced a mutation (Kir6.2-C166S) which increases P_{open} of K_{ATP} and decreases sensitivity of the channel to block by nucleotides (*Trapp et al., 1998*). C166 is located near the bundle-crossing gate of Kir6.2 (Figure 3A). Other mutations at this site cause neonatal diabetes (*Flanagan et al., 2006*; *Gloyn et al., 2006*).

In unroofed membranes, Kir6.2*-C166S-GFP + SUR1 bound TNP-ATP with an EC_{50} very similar to that of Kir6.2*-GFP + SUR1 (Figure 3B, 32.0 μ M and 25.6 μ M, respectively), which suggests only a small change in nucleotide affinity. This is an unexpected finding, as one might expect that an increase in P_{open} would allosterically cause a decrease in the apparent affinity for inhibitory nucleotide binding. To resolve this conflict, we again turned to PCF (Figure 3C,D). Rundown was much slower for Kir6.2*-C166S-GFP + SUR1, which may reflect the increased P_{open} of this construct. Measuring current inhibi-

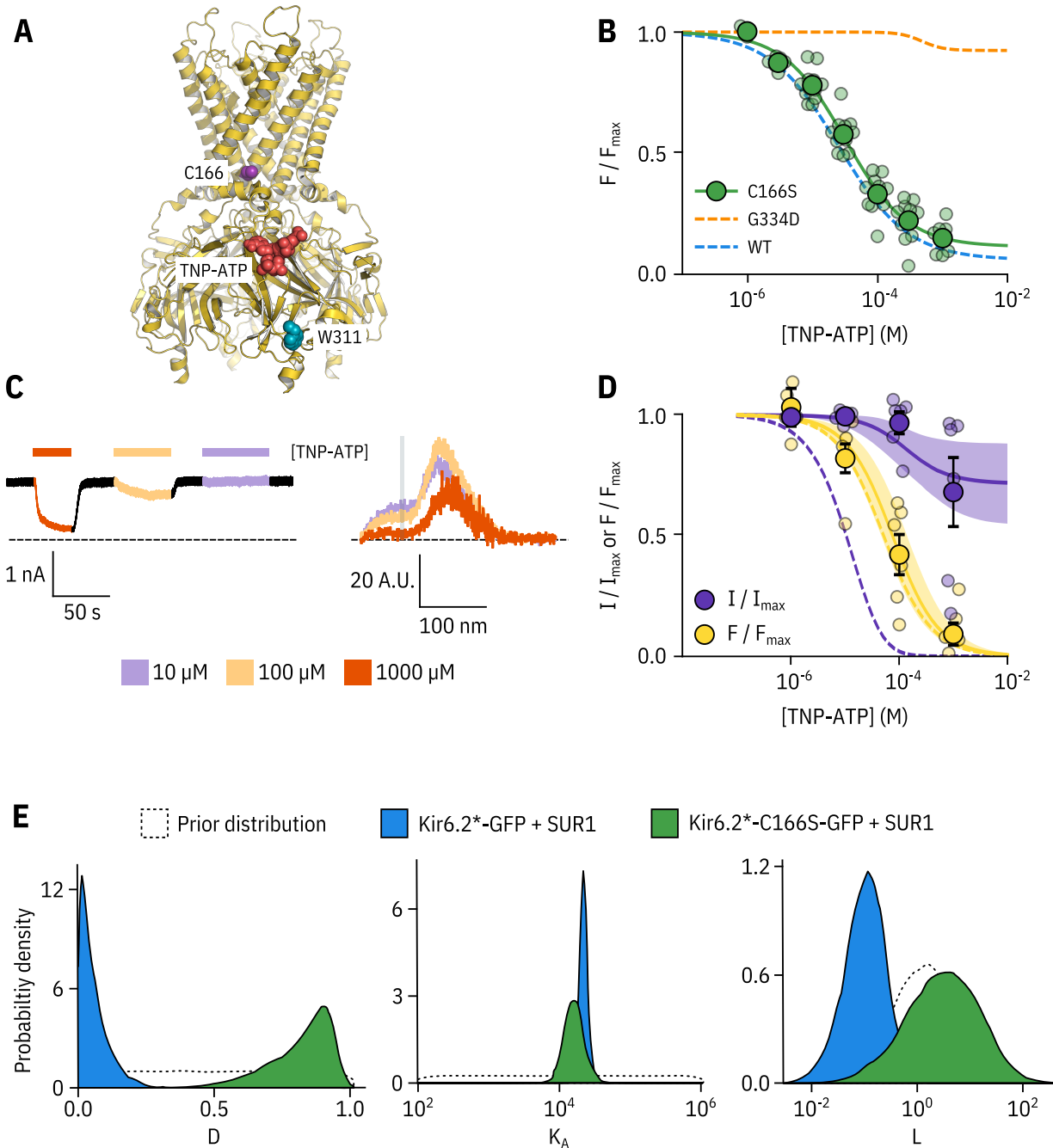


Figure 3. Kir6.2-C166S disrupts current inhibition, not nucleotide binding.

Figure 3. Kir6.2-C166S disrupts current inhibition, not nucleotide binding. **A.** Cartoon (from PDB accession #6BAA) showing the location of Kir6.2-C166 (purple) relative to the inhibitory nucleotide binding site (TNP-ATP from PDB accession #5XW6 shown in red). W311 is shown as blue spheres. **B.** Concentration dependence of TNP-ATP binding to unroofed membrane fragments expressing Kir6.2*-C166S-GFP + SUR1 shown in green, expressed as quenching of ANAP fluorescence. The Hill fits shown previously for Kir6.2*-GFP + SUR1 and Kir6.2*-G334D-GFP are shown in blue and orange dashed curves, respectively. Kir6.2*-C166S-GFP + SUR1: $EC_{50} = 32.0 \mu M$, $h = 0.92$, $E_{max} = 0.96$, $n = 12$. **C.** Representative current and fluorescence traces recorded simultaneously from an excised patch expressing Kir6.2*-C166S-GFP + SUR1. Exposure to different concentrations of TNP-ATP are shown by colour. **D.** Concentration-response ($n = 6$) for TNP-ATP inhibition of Kir6.2*-C166S-GFP + SUR1 currents (I/I_{max}) and for quenching of ANAP fluorescence (F/F_{max}). Data were fit with the MWC-type model. Solid curves represent the median fits and shaded areas indicate the 95% quantile intervals. Dashed curves represent the previous median fits of the MWC-type model to the Kir6.2*-GFP + SUR1 data from Figure 2D. Parameter estimates are reported in Table 3. **E.** Posterior probability distributions for the full MWC-type model fit to Kir6.2*-C166S-GFP + SUR1 or Kir6.2*-GFP + SUR1 (data from Figure 2F) overlaid on the prior probability distribution.

Figure 3 – figure supplement 1. Fixing the L parameter does not affect the other two parameters.

²³⁰ tion in combination with nucleotide binding confirmed that whereas the apparent nu-
²³¹ cleotide affinity was unchanged by the C166S mutation, current inhibition occurred at
²³² much higher concentrations compared to binding (Figure 3D). How can we explain this
²³³ paradox? Fits of the data with our MWC-type model (Figure 3D,E) suggest that, in ad-
²³⁴ dition to the expected effect on L , the C166S mutation profoundly affects the ability of
²³⁵ bound ligand to close the channel (D) without affecting K_A (Figure 3E, Table 3). We pro-
²³⁶ pose that, in addition to increasing the P_{open} of the channel, C166 is also important in the
²³⁷ transduction pathway from the inhibitory nucleotide binding site on Kir6.2 to the channel
²³⁸ gate.

²³⁹ **Exploring the effect of SUR1 on nucleotide inhibition of K_{ATP} .** SUR1 plays a com-
²⁴⁰ plex role in the regulation of Kir6.2. It increases the P_{open} of the channel and allows for
²⁴¹ the activation of the channel by Mg-nucleotides (**Nichols et al., 1996; Tucker et al., 1997;**
²⁴² **Babenko and Bryan, 2003; Chan et al., 2003; Fang et al., 2006**). However, it also increases
²⁴³ the sensitivity of Kir6.2 to nucleotide inhibition (**Babenko and Bryan, 2003; Chan et al.,**

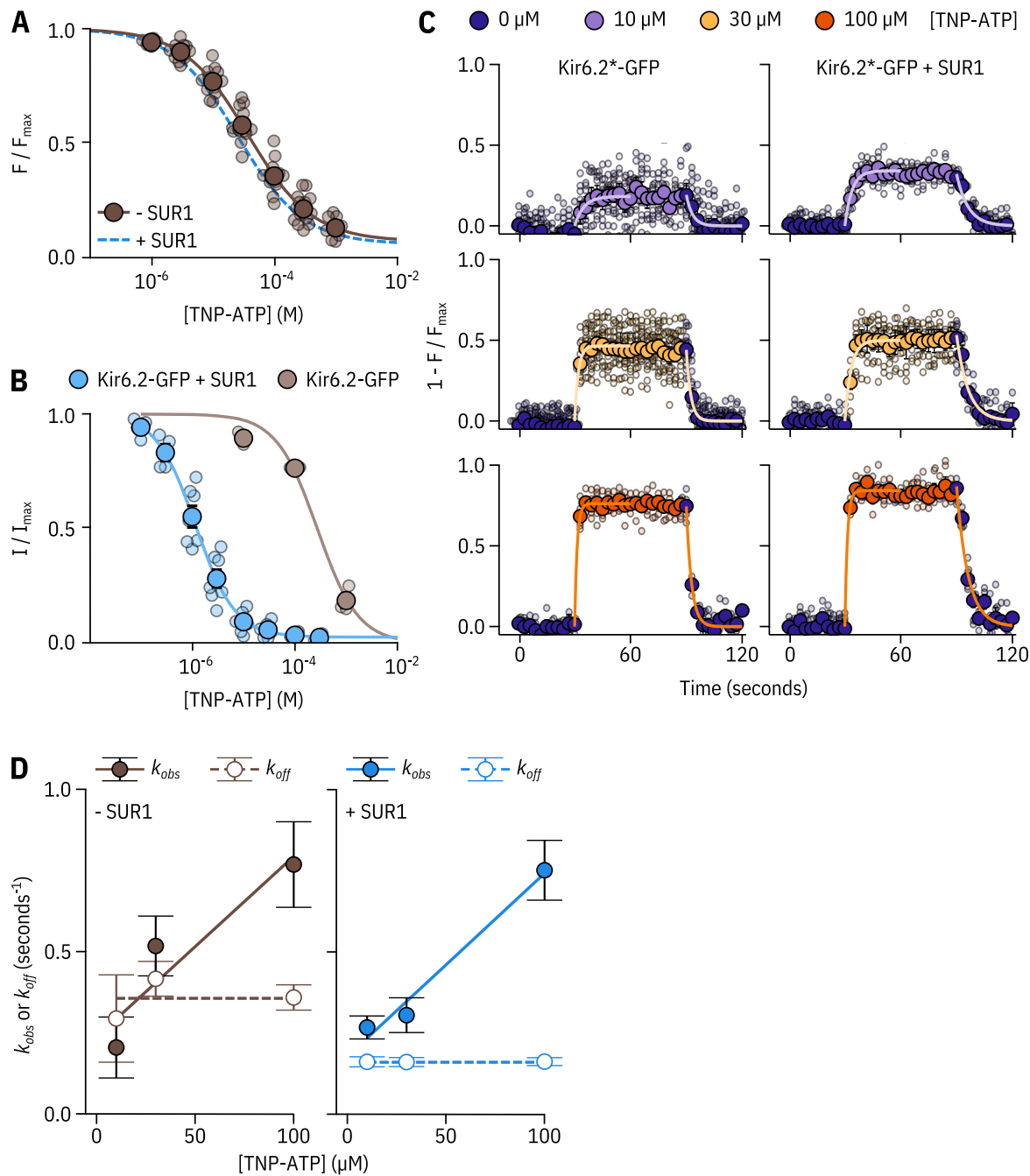


Figure 4. SUR1 affects the apparent affinity for and kinetics of nucleotide binding to Kir6.2.

Figure 4. SUR1 affects the apparent affinity for and kinetics of nucleotide binding to Kir6.2. **A.** Concentration dependence of TNP-ATP binding to unroofed membrane fragments expressing Kir6.2*-GFP without SUR1 (brown), expressed as quenching of ANAP fluorescence. The smooth curve is a descriptive Hill fit. Kir6.2*-GFP (no SUR1): $EC_{50} = 37.6 \mu M$, $h = 0.83$, $E_{max} = 0.92$, $n = 14$. The Hill fit to Kir6.2*-GFP + SUR1 is shown as a blue dashed curve. **B.** Concentration-response curve for TNP-ATP inhibition of Kir6.2-GFP (no ANAP label) without or with co-expression of SUR1, measured in excised, inside-out patches. Kir6.2-GFP + SUR1: $EC_{50} = 1.17 \mu M$, $h = 1.14$, $E_{max} = 0.97$, $n = 7$; Kir6.2-GFP (no SUR1): $EC_{50} = 273 \mu M$, $h = 1.09$, $E_{max} = 1.00$, $n = 3$. **C.** Time-courses of TNP-ATP binding and unbinding to Kir6.2*-GFP expressed in unroofed membrane fragments in the presence or absence of SUR1. Data are displayed as $1 - F/F_{max}$ so that upward deflections indicate binding and downward deflections indicate unbinding. Small data points represent individual experiments. Overlaid are larger points representing the mean \pm standard error at each time point. The smooth curves are single exponential fits to the wash-on or wash-off of a given concentration of TNP-ATP. **D.** Rate constants (k_{obs} and k_{off}) from the exponential fits as in **C** are plotted as functions of the TNP-ATP concentration. Linear fits to k_{obs} were performed using equation 3. Kir6.2*-GFP (no SUR1): $k_{on} = 5560 M^{-1} s^{-1} \pm 2180 M^{-1} s^{-1}$, $k_{off} = 0.24 s^{-1} \pm 0.13 s^{-1}$, $n = 2-6$ per concentration. Kir6.2*-GFP + SUR1: $k_{on} = 5640 M^{-1} s^{-1} \pm 812 M^{-1} s^{-1}$, $k_{off} = 0.18 s^{-1} \pm 0.05 s^{-1}$, $n = 3-4$ per concentration. Dashed lines indicate the mean rates measured for wash-off experiments (k_{off}) from all test concentrations combined. Kir6.2*-GFP (no SUR1): $k_{off} = 0.36 s^{-1} \pm 0.04 s^{-1}$. Kir6.2*-GFP + SUR1: $k_{off} = 0.16 s^{-1} \pm 0.0004 s^{-1}$.

244 2003; Fang et al., 2006). To understand the effect of SUR1 on nucleotide inhibition of K_{ATP},
 245 we expressed Kir6.2*-GFP in the absence of SUR1 in unroofed membranes and measured
 246 TNP-ATP binding (Figure 4A). We found only a small increase (approximately 1.5-fold) in
 247 apparent EC₅₀ compared to the same construct in the presence of SUR1 (37.6 μM and
 248 25.6 μM respectively). Unfortunately, we were unable to achieve high enough expression
 249 of Kir6.2*-GFP alone to carry out PCF experiments in the absence of SUR1. However,
 250 we were able to measure currents from unlabelled Kir6.2-GFP alone (Figure 4B). As ex-
 251 pected Kir6.2-GFP alone was much less sensitive to inhibition by TNP-ATP than Kir6.2-GFP
 252 + SUR1.

253 To determine whether SUR1 had complex effects on nucleotide binding that were not
 254 revealed in equilibrium binding experiments, we measured the time-course of TNP-ATP
 255 binding and unbinding to Kir6.2*-GFP expressed in unroofed membranes in the absence
 256 and presence of SUR1 (Figure 4C). We fit the apparent on- (k_{obs}) and off-rates (k_{off}) for dif-
 257 ferent concentrations of TNP-ATP to single exponential decays (equation 1). As expected,
 258 the off-rate was independent of [TNPATP]. We determined k_{on} from the slope of linear
 259 fits to k_{obs} as a function of nucleotide concentration, where $k_{obs} = k_{on} * [TNPATP] + k_{off}$
 260 (Figure 4D). k_{on} for TNP-ATP binding was nearly identical in the presence and absence of
 261 SUR1 (5641 M⁻¹ s⁻¹ vs. 5564 M⁻¹ s⁻¹, respectively). However, the mean k_{off} was roughly
 262 twice as fast in the absence of SUR1 (0.36 s⁻¹ in the absence of SUR1 vs. 0.16 s⁻¹ in the
 263 presence of SUR1). Measuring k_{on} and k_{off} also provided an independent measure of
 264 EC₅₀, if we assume a single-step process with EC₅₀ given by k_{off}/k_{on} . Using this method,
 265 we calculated the EC₅₀ for Kir6.2*-GFP + SUR1 to be 28.3 μM, quite close to the 25.6 μM
 266 derived from steady-state measurements. The EC₅₀ calculated from the TNP-ATP bind-
 267 ing kinetics for Kir6.2*-GFP in the absence of SUR1 was 64.0 μM, higher than the value
 268 of 37.6 μM derived from steady-state measurements. We believe this discrepancy arises
 269 from the variability in our rate measurements. Nevertheless, the two-fold decrease in
 270 k_{off} for TNP-ATP in the presence of SUR1 suggests that SUR1 stabilises nucleotide bind-
 271 ing to Kir6.2. However, these binding measurements do not rule out an indirect, allosteric

²⁷² effect of SUR1 on nucleotide binding. To explore the effect of SUR1 more rigorously, we
²⁷³ again turned to PCF.

²⁷⁴ As Kir6.2*-GFP expression in the absence of SUR1 was not sufficient for PCF record-
²⁷⁵ ings, we took a mutational approach to better understand the role of SUR1 in inhibitory
²⁷⁶ nucleotide binding. SUR1-K205 is located in the L0 linker of SUR1, which connects the
²⁷⁷ first set of transmembrane domains (TMD0) to the ABC core structure (Figure 1A, Figure
²⁷⁸ 5A; *Martin et al. (2017); Puljung (2018)*). This loop is adjacent to the inhibitory nucleotide-
²⁷⁹ binding site on Kir6.2 and the interface between neighbouring Kir6.2 subunits. Mutations
²⁸⁰ at K205 were previously shown to reduce sensitivity of K_{ATP} to nucleotide-dependent in-
²⁸¹ hibition (*Pratt et al., 2012; Ding et al., 2019*). Other mutations in L0 are associated with
²⁸² neonatal diabetes (*Ashcroft et al., 2017*) and PHHI (*Snider et al., 2013*).

²⁸³ We introduced a charge neutralization (alanine, K205A) and a charge reversal (gluta-
²⁸⁴ mate, K205E) mutation at this position and measured simultaneous nucleotide binding
²⁸⁵ and current inhibition with PCF (Figure 5B,C,D). The binding and inhibition curves for TNP-
²⁸⁶ ATP almost perfectly overlaid for the SUR1-K205A mutant (Figure 5C). The same was also
²⁸⁷ true for SUR1-K205E (Figure 5D). Data were fit with the MWC-type model as before. Mu-
²⁸⁸ tating K205 to an alanine or a glutamate resulted in an apparent decrease in nucleotide
²⁸⁹ binding affinity (Figure 5C,D,E). This was reflected by a decrease in the estimated K_A for
²⁹⁰ TNP-ATP, which correlated with the degree of conservation of the mutation, i.e. we ob-
²⁹¹ served a larger effect for the charge reversal compared to the charge neutralization mu-
²⁹² tation (Figure 5E). However, in addition to direct effects of K205 on nucleotide binding,
²⁹³ we also observed a shift in D for both mutations (Figure 5E). This suggests a dual role for
²⁹⁴ SUR1 in K_{ATP} inhibition, both in contributing to nucleotide binding and in stabilizing the
²⁹⁵ nucleotide-bound closed state.

²⁹⁶ Discussion

²⁹⁷ We have developed a novel approach that allows for site-specific measurement of nu-
²⁹⁸ cleotide binding to K_{ATP} and concomitant measurements of channel current. Perform-

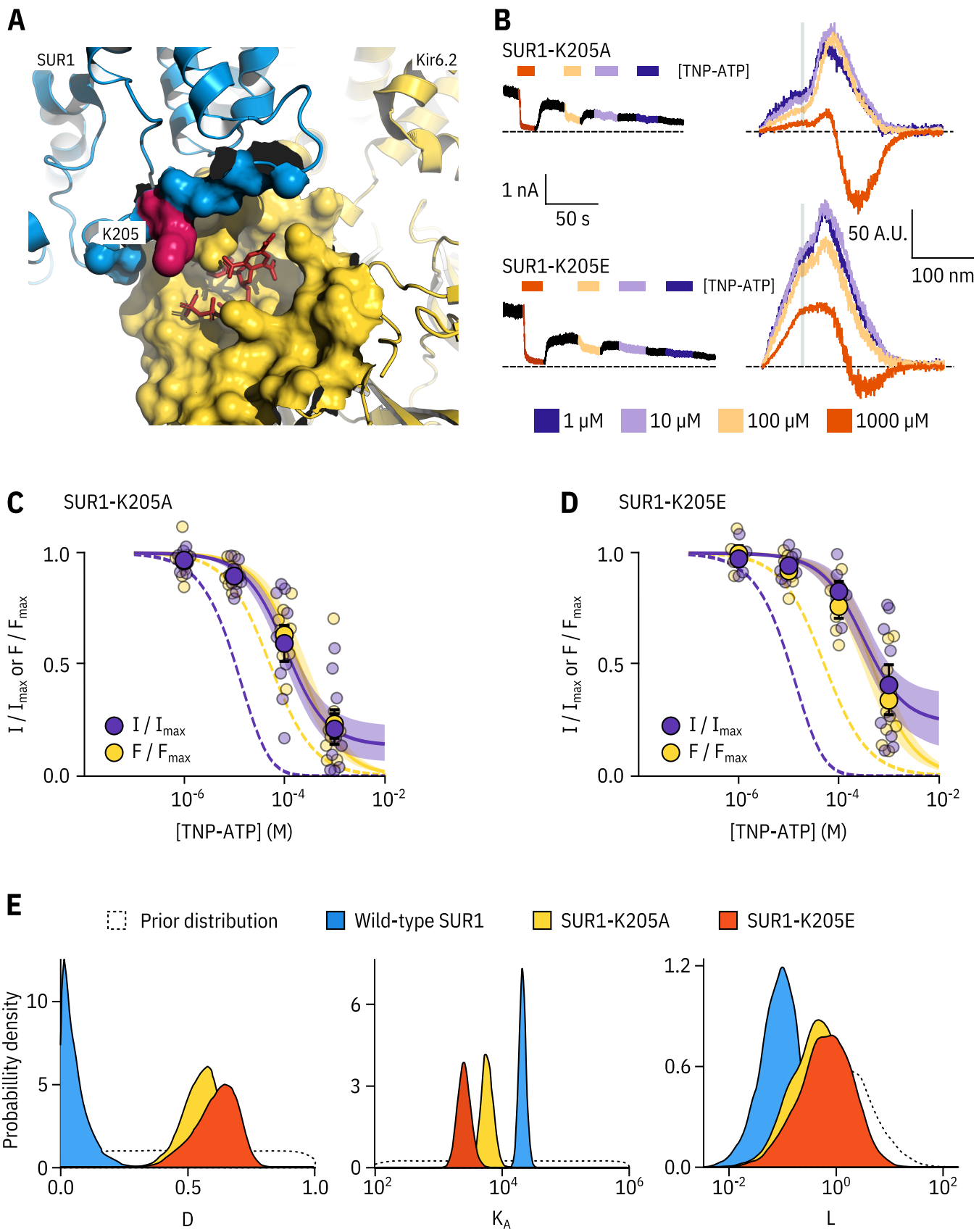


Figure 5. SUR1-K205 modulates both nucleotide affinity and inhibition of Kir6.2.

Figure 5. SUR1-K205 modulates both nucleotide affinity and inhibition of Kir6.2. **A.** Hydrophobic surface representation of Kir6.2 (yellow, PDB accession #6BAA) and SUR1 (blue, PDB accession #6PZI). Residue K205 on SUR1 is highlighted in pink. As this residue was built as an alanine in the structure, we used the mutagenesis tool in PyMol to insert the native lysine residue. A docked TNP-ATP molecule is shown in red. **B.** Representative current and fluorescence traces acquired simultaneously from excised patches expressing Kir6.2*-GFP with SUR1-K205A or SUR1-K205E. **C,D.** Concentration-response for TNP-ATP inhibition of currents (I/I_{max}) and for quenching of ANAP fluorescence (F/F_{max}) in excised inside-out membrane patches expressing Kir6.2*-GFP + SUR1-K205A (**C**, $n = 9$) or Kir6.2*-GFP + SUR1-K205E (**D**, $n = 9$). Data were fit to the MWC-type model. Solid curves represent the median fits and shaded areas indicate the 95% quantile intervals. Fits to Kir6.2*-GFP + wild-type SUR1 are shown as dashed curves. **E.** Posterior probability distributions for the full MWC-type model fit to Kir6.2*-GFP co-expressed with wild-type SUR1 (fits from Figure 2), SUR1-K205A and SUR1-K205E overlaid on the prior probability distribution.

Figure 5 – figure supplement 1. Fixing the L parameter does not drastically affect the fits to the SUR1-K205A or SUR1-K205E data.

Figure 5 – figure supplement 2. Comparing the ability of each model to explain the data.

299 ing these measurements simultaneously allowed us to examine nucleotide regulation of
 300 K_{ATP} function in great detail. We used a Bayesian approach to fit models to our combined
 301 fluorescence/current data sets to extract meaningful functional parameters with a min-
 302 imum of prior assumptions. Such insights would not be possible from experiments in
 303 which macroscopic currents or binding were measured in isolation.

304 PCF has been used successfully by other labs to simultaneously measure ligand bind-
 305 ing and gating in HCN channels (*Biskup et al., 2007; Kusch et al., 2010; Wu et al., 2011*).

306 These groups measured fluorescence from a cyclic nucleotide analogue that increased its
 307 quantum yield when bound, minimizing background fluorescence from unbound ligand.

308 Additional background subtraction could be performed by imaging the patches using
 309 confocal microscopy such that a region corresponding to the patch membrane could be
 310 computationally selected, thus omitting background fluorescence from the surrounding
 311 solution (*Biskup et al., 2007; Kusch et al., 2010*). In our PCF experiments, we used a FRET-
 312 based approach to measure ligand binding. We acquired fluorescence emission spectra,
 313 such that donor fluorescence could be separated from acceptor fluorescence by wave-

length. This allowed us to directly assess binding from the quenching of donor fluorescence, which was specific to K_{ATP} . FRET also provided the spatial sensitivity necessary to discriminate between nucleotide binding directly to Kir6.2 and to the nucleotide-binding sites of SUR1. We assume that any TNP-ATP bound non-specifically to our membranes would be too far from Kir6.2 to cause appreciable FRET. This assumption was confirmed by the lack of FRET between TNP-ATP and a Kir6.2*-GFP mutant (G334D), in which nucleotide binding was severely disrupted (Figure 1H).

Previous studies have suggested that K_{ATP} inhibition follows an MWC-type model (*Trapp et al., 1998; Enkvetachakul and Nichols, 2003; Drain et al., 2004; Craig et al., 2008; Vedorato et al., 2015*). The majority of this earlier work was performed using single-channel measurements of mutated and/or concatenated channel subunits. In this study, we confirm these results using minimally perturbed channels with nucleotide sensitivity similar to that of wild-type K_{ATP} (Figure 1—Figure supplement 2A). By using an MCMC approach to model fitting, we can also evaluate our models to assess how well the derived parameters were determined by the data. MCMC fits provide a basis for determining credible intervals for our parameter estimates. This allows for direct comparison of values derived from wild-type and different mutant constructs.

Although we did not explicitly include the effects of PIP_2 on K_{ATP} gating in our model formulations, we assumed that the effects of PIP_2 on P_{open} were implicitly modelled in our parameter L ; i.e. rundown due to dissociation of PIP_2 manifests as a decrease in L rather than a change in the number of channels. Although we were able to extract identifiable parameter estimates for L , D and K_A , our estimates of L for each model we considered were appreciably less well constrained than for the other parameters. We expect that this uncertainty arises from measuring a heterogeneous population of channels with regard to PIP_2 binding. Fixing L to values derived from the literature (Figure 2—Figure supplement 1, Figure 3—Figure supplement 1, Figure 5—Figure supplement 1, Figure 5—Figure supplement 2) allowed us to extract estimates for D and K_A that were functionally identical to those derived from unconstrained fits, suggesting that the uncertainty of L

342 does not affect our inferences for these other parameters. Therefore, PCF represents a
 343 robust means to compare K_A and D between different mutated K_{ATP} constructs without
 344 worrying about the confounding effects of rundown.

345 Previous studies suggest that, whereas K_{ATP} closure occurs via a concerted mecha-
 346 nism, individual nucleotide binding events at Kir6.2 are not equivalent (*Markworth et al.,*
 347 **2000**). Earlier attempts to determine the stoichiometry of inhibitory nucleotide binding
 348 to Kir6.2 (i.e. how many ATPs must bind to induce channel closure) have produced mod-
 349 els ranging from those in which binding of a single nucleotide completely shuts K_{ATP} to
 350 an MWC-type model in which each binding event is independent and contributes equally
 351 to channel closure (*Trapp et al., 1998; Markworth et al., 2000; Enkvetachakul and Nichols,*
 352 **2003; Drain et al., 2004; Wang et al., 2007; Craig et al., 2008; Vedovato et al., 2015**). To
 353 resolve this controversy, we fit our data with both single-binding and MWC-type models.
 354 At very low values for D , such as we derived from our experiments, the predictions of
 355 both models are functionally very similar. Even in our MWC-type model, we expect most
 356 K_{ATP} channels to be closed when just one molecule of nucleotide is bound.

357 It has been proposed that there is direct negative cooperativity between binding events
 358 at different subunits on Kir6.2 (*Wang et al., 2007*). We fit our data to an extended MWC-
 359 type model including an additional free parameter (C), representing negative binding
 360 cooperativity between subunits (Figure 2—Figure supplement 2). Not surprisingly this
 361 model improved the fit to our data as assessed by the Bayes factor, which represents
 362 the marginal likelihood of one model over another to explain our observations (*Wagen-*
 363 *makers, 2007; Gronau et al., 2017*). We also tested the cooperative model using approx-
 364 imate leave-one-out cross validation, which assesses the ability of a model to predict
 365 new or out-of-sample data using in-sample fits. Although in this work, we are primarily
 366 concerned with the inferences made from our fits, the ability of a model to make predi-
 367 cations is a good measure of its usefulness. Based on this criterion, the cooperative model
 368 has no more predictive accuracy than either the MWC-type model or the single-binding
 369 model. Therefore, the inclusion of an additional free parameter is not justified. Further-

370 more, whereas the cooperative model yielded good fits with identifiable parameters for
 371 Kir6.2*-GFP + SUR1 channels, it failed to do so for all the mutants considered. Thus, this
 372 model did not allow for direct comparison between constructs. However, it remains a
 373 possibility that these mutations function in part by abolishing binding cooperativity be-
 374 tween subunits.

375 We performed all our experiments on mutated, tagged channels using a fluorescent
 376 derivative of ATP. This allowed us to fit mechanistic models and readily compare between
 377 mutated constructs that affect nucleotide inhibition of K_{ATP} . This raises an obvious ques-
 378 tion: how relevant are our findings to inhibition of wild-type K_{ATP} by ATP? In a previous
 379 paper, we estimated D and K_A from an MWC-type model based on fits to published data
 380 for ATP inhibition of wild-type Kir6.2 + SUR1 (*Proks et al., 2010; Vedovato et al., 2015*).
 381 The value we obtained for D (0.03) was quite similar to that we report here from our PCF
 382 measurements (0.04). We also obtained a similar estimate for K_A in our previous model
 383 ($3.0 \times 10^4 \text{ M}^{-1}$ vs $2.1 \times 10^4 \text{ M}^{-1}$ from our PCF experiments). Despite obtaining similar pa-
 384 rameters, past experiments in which only ionic currents were measured, did not allow us
 385 to distinguish between competing gating models. Measuring currents and fluorescence
 386 simultaneously allowed for better model selection and aided in our ability to identify con-
 387 strained parameters.

388 We compared the parameters derived for inhibitory nucleotide binding to those esti-
 389 mated for nucleotide activation of K_{ATP} based on experiments in which currents and bind-
 390 ing were measured in separate preparations (*Puljung et al., 2019*). In those experiments,
 391 we estimated a value for E , the factor by which binding of MgTNP-ADP to SUR1 stabilized
 392 channel opening, of 2.2. Although this value was derived using a different nucleotide, it
 393 still provides an approximate basis for comparing the coupling of nucleotide stimulation
 394 through SUR1 to nucleotide inhibition via binding to Kir6.2. If both activation and inhibi-
 395 tion proceed via MWC-type models, the open closed equilibrium at saturating nucleotide
 396 concentrations is given by L multiplied by E^4 or D^4 , respectively. The degree of stabiliza-
 397 tion of the open state of K_{ATP} can be calculated as $-RT \ln E^4$ for activation. Stabilization

398 of the closed state is given by $-RT \ln D^4$. Based on our observations, saturating concen-
 399 trations of MgTNP-ADP stabilized the open state by $-1.9 \text{ kcal mol}^{-1}$ (-7.9 kJ mol^{-1}). At
 400 saturating concentrations, TNP-ATP stabilized the closed state of K_{ATP} by $-7.6 \text{ kcal mol}^{-1}$
 401 (31.8 kJ mol^{-1}). Thus, at conditions under which both excitatory and inhibitory nucleotide
 402 binding sites are saturated, inhibition dominates, which is consistent with published mea-
 403 surements of wild-type K_{ATP} in the presence of Mg^{2+} (). In our previous study, we es-
 404 timated K_A for MgTNP-ADP binding to the stimulatory second nucleotide binding site
 405 of SUR1 to be $5.8 \times 10^4 \text{ M}^{-1}$ ($K_D = 17 \mu\text{M}$), higher affinity than the K_A we report here
 406 for TNP-ATP binding to the inhibitory site on Kir6.2 ($2.1 \times 10^4 \text{ M}^{-1}$, $K_D = 48 \mu\text{M}$). Higher
 407 affinity binding to the stimulatory site may explain the ability of MgADP to increase K_{ATP}
 408 currents in the presence of ATP (Gribble et al., 1998). This phenomenon may also explain
 409 the bell-shaped MgADP concentration-response curve for K_{ATP} , which shows an increase
 410 in current at low concentrations, followed by inhibition at higher concentrations (Proks
 411 et al., 2010; Vedovato et al., 2015). Future experiments in which activation and inhibition
 412 are measured by PCF for the same ligand will allow us to model the complex response
 413 of K_{ATP} under conditions where all three nucleotide binding sites simultaneously affect
 414 channel gating (i.e. in the presence of Mg^{2+}).

415 Mutations that cause neonatal diabetes reduce the sensitivity of K_{ATP} to nucleotide in-
 416 hibition, and reduction in nucleotide sensitivity is broadly correlated with disease severity
 417 (McTaggart et al., 2010). We studied two residues on Kir6.2 that have been implicated
 418 in diabetes and have been proposed to affect nucleotide sensitivity via different mecha-
 419 nisms. We find that G334D drastically reduced the apparent affinity for nucleotide bind-
 420 ing to K_{ATP} in unroofed membranes. In our MWC-type models, this could only be ex-
 421 plained by a dramatic decrease in K_A . This corroborates earlier hypotheses that mutat-
 422 ing G334 directly disrupts inhibitory nucleotide binding to Kir6.2 (Drain et al., 1998). Due
 423 to poor expression, we were unable to test this construct using PCF. Therefore, we could
 424 not obtain accurate estimates of K_A and D .

425 In contrast to G334D, the C166S mutation does not directly affect nucleotide binding

426 to Kir6.2, but rather disrupts the ability of bound nucleotide to close the channel. This
427 contributes to the decreased nucleotide sensitivity which was previously attributed solely
428 to an increased P_{open} . In the future, we hope to use this rigorous approach to assess a
429 whole panel of neonatal diabetes mutations in Kir6.2 to better understand the mecha-
430 nism by which they cause disease.

431 Using PCF allowed us to probe more deeply into the role of SUR1 in regulating nu-
432 cleotide inhibition of K_{ATP} . The cytoplasmic L0 loop of SUR1 was previously implicated
433 in modulation of P_{open} and nucleotide sensitivity of Kir6.2 (**Babenko and Bryan, 2003;**
434 **Chan et al., 2003; Pratt et al., 2012**). We find that, in addition to directly contributing
435 to tighter nucleotide binding at Kir6.2, SUR1 plays a critical role in preferentially stabil-
436 ising the closed state of the channel when nucleotides are bound. Whereas a single
437 nucleotide-binding event is sufficient for channel closure when Kir6.2 is associated with
438 wild-type SUR1, mutating residue K205 reduced the ability of a single nucleotide to close
439 the channel. This difference manifests in both our MWC-type and single-binding models.

440 In addition to providing mechanistic insights into disease-associated mutations in
441 Kir6.2, our PCF-based approach allows us to probe the interactions between Kir6.2 and
442 SUR1 on two different levels. As we show here, we can use this method to examine the
443 effects of SUR1 on inhibitory nucleotide binding to Kir6.2. We can also adapt this method
444 to study activation of Kir6.2 by nucleotides bound to the stimulatory sites on SUR1. Mu-
445 tations in SUR1 that cause neonatal diabetes may do so by disrupting inhibitory bind-
446 ing/gating or enhancing the stimulatory effects of nucleotides. The formalism developed
447 in this study provides a rigorous way to mechanistically assess the effects of these muta-
448 tions. Our approach should be readily adaptable to the study of other nucleotide-gated
449 channels including the cystic fibrosis transmembrane conductance regulator (CFTR, also
450 an ABC-family protein) and purinergic P2X receptors.

451 **Materials and Methods**

452 **Key resources table.**

Reagent (species) or resource	type	Designation	Source or refer- ence	Identifiers
Cell line		HEK-293T	LGC Standards (ATCC CRL-3216)	
Transfected construct (<i>Escherichia. coli</i>)		pANAP	Addgene	
Transfected construct		pcDNA4/TO	Addgene	
Transfected construct (<i>Aequorea victoria</i>)		pCGFP_EU	Gouaux Laboratory (Vollum Institute, Portland OR USA)	
Transfected construct (<i>Homo sapiens</i>)		peRF1-E55D	Chin Laboratory (MRC Laboratory of Molecular Biology, Cambridge UK)	
453	Antibody	Anti-HA High Affinity; Rat monoclonal antibody (clone 3F10)	Roche	(Roche Cat# 11867423001, RRID:AB_10094468)
Antibody		Peroxidase-AffiniPure Goat Anti-Rat IgG (H + L) antibody	Jackson ImmunoResearch Labs	(Jackson ImmunoResearch Labs Cat# 112-035-003, RRID:AB_2338128)
Chemical compound, drug		trinitrophenyl-ATP (TNP-ATP)	Jena Bioscience (Jena, Germany)	
Chemical compound, drug		L-3-(6-acetyl naphthalen-2-ylamino)-2-aminopropionic acid	Asis Chemicals (Waltham, MA)	

454 **Molecular biology.**

455 Human Kir6.2 and SUR1 were subcloned into pcDNA4/TO and pCGFP_EU vectors for ex-
 456 pression of wild-type and GFP-tagged constructs, respectively. pcDNA4/TO and pANAP
 457 were obtained from Addgene. peRF1-E55D and pCGFP_EU were kind gifts from the Chin
 458 Laboratory (MRC Laboratory of Molecular Biology, Cambridge, UK) and the Gouaux Lab-
 459 oratory (Vollum Institute, Oregon, USA) respectively. Amber stop codons and point mu-
 460 tations were introduced using the QuikChange XL system (Stratagene; San Diego, CA). All

⁴⁶¹ constructs were confirmed by DNA sequencing (DNA Sequencing and Services, University
⁴⁶² of Dundee, Scotland).

⁴⁶³ Cell culture and channel expression.

⁴⁶⁴ HEK-293T cells were obtained from and verified/tested for mycoplasma by LGC standards
⁴⁶⁵ (ATTC CRL-3216, Middlesex, UK). Our working stock tested negative for mycoplasma con-
⁴⁶⁶ tamination using the MycoAlert Mycoplasma Detection Kit (Lonza Bioscience; Burton on
⁴⁶⁷ Trent, UK). Cells were plated onto either poly-L-lysine coated borosilicate glass coverslips
⁴⁶⁸ (VWR International; Radnor, PA) or poly-D-lysine coated glass-bottomed FluoroDishes
⁴⁶⁹ (FD35-PDL-100, World Precision Instruments). ANAP-tagged Kir6.2 constructs were la-
⁴⁷⁰ belled using amber stop codon suppression as described by Chatterjee et al (*Chatterjee*
⁴⁷¹ *et al., 2013*). Transfections were carried out 24 hours after plating using Transit-LT1
⁴⁷² (Mirus Bio LLC; Madison, WI) at a ratio of 3 µl per µg of DNA. Unless specified otherwise,
⁴⁷³ all transfections included a Kir6.2 construct with an amber stop codon (TAG) at position
⁴⁷⁴ 311 (Kir6.2-W311^{TAG}), SUR1, pANAP and eRF1-E55D in the ratio 0.5:1.5:1:1. Transfected
⁴⁷⁵ cells cultured in Dulbecco's Modified Eagle Medium (Sigma; St. Louis, MO) + 10% foetal
⁴⁷⁶ bovine serum, 100 U ml⁻¹ penicillin and 100 µg ml⁻¹ streptomycin (Thermo Fisher Scien-
⁴⁷⁷ tific; Waltham, MA) supplemented with 20 mM ANAP (free acid, AsisChem; Waltham, MA).
⁴⁷⁸ Cells were incubated at 33 °C and in the presence of 300 µM tolbutamide to enhance
⁴⁷⁹ protein expression and channel trafficking to the plasma membrane (*Yan et al., 2007*;
⁴⁸⁰ *Lin et al., 2015*). eRF1-E55D was included to increase efficiency of ANAP incorporation
⁴⁸¹ (*Schmied et al., 2014*). Experiments were carried out 2-4 days after transfection. We also
⁴⁸² expressed constructs labelled with ANAP at positions I182, F183, F198, and I210. Kir6.2-
⁴⁸³ F183*, Kir6.2-F198*, and Kir6.2-I210* co-expressed with SUR1 did not produce sufficient
⁴⁸⁴ currents for subsequent experimentation. Mutations at I182 are known to produce pro-
⁴⁸⁵ found effects on nucleotide inhibition of K_{ATP} (*Li et al., 2000*). Thus, we did not consider
⁴⁸⁶ this site for further experimentation.

487 **Western blots.**

488 Transfected HEK-293T cells grown in 6-well plates were harvested in cold PBS (Life Tech-
489 nologies Limited; Paisley, UK), pelleted at 0.2 x g for 2.5 minutes and resuspended in lysis
490 buffer containing 0.5% Triton X-100, 100 mM potassium acetate, and a cOmplete pro-
491 tease inhibitor tablet (1 tablet/50 ml, Roche; Basel, Switzerland), buffered to pH 7.4. Af-
492 ter a 30-minute benzonase (Sigma) treatment at room temperature, samples were mixed
493 with a DTT containing reducing agent and loading buffer (NuPAGE, Invitrogen; Carlsbad,
494 CA) and run on a precast Bis-Tris 4-12% poly-acrylamide gel at 200 V for 40 minutes. Pro-
495 teins were wet transferred overnight onto polyvinylidene difluoride (PVDF) membranes
496 (Immobilon P, Merck Millipore; Burlington, VT) in 25 mM Tris, 192 mM glycine, 20% methanol,
497 and 0.1% SDS at 10 V on ice. Membranes were blocked with 5% milk in TBS-Tw (150 mM
498 NaCl, 0.05% Tween 20, 25 mM mM Tris, pH 7.2) before staining for 30 minutes with a
499 1:1000 dilution of rat anti-HA monoclonal antibody in TBS-Tw (clone 3F10, Roche). After
500 washing with TBS-Tw, membranes were incubated for 30 minutes with a 1:20,000 dilu-
501 tion of HRP-conjugated goat anti-rat polyclonal antibodies in TBS-Tw (Jackson ImmunoRe-
502 search; Ely, UK). Detection was performed using the SuperSignal West Pico Chemilumi-
503 nescent Substrate (Thermo Fisher) and a C-DiGit Blot Scanner (Licor Biosciences; Lincoln,
504 NE). Analysis was performed using custom code written in Python.

505 To confirm our ability to express full-length Kir6.2*-GFP, we performed western blots
506 for HA-tagged Kir6.2 constructs in detergent-solubilized HEK-293T cells (Figure 1—Figure
507 supplement 1C). The HA tag plus a short linker (YAYMEKGITDLAYPYDVPDY) was inserted
508 in the extracellular region following helix M1 of Kir6.2 between L100 and A101. Transfec-
509 tion of wild-type Kir6.2-HA or Kir6.2-HA-GFP resulted in two bands on the western blots.
510 The upper bands were close to the expected sizes for full-length Kir6.2-HA and Kir6.2-HA-
511 GFP (46 kDa and 77 kDa, respectively).

512 We consistently observed a lower molecular weight band as well. This band must cor-
513 respond to an N-terminally truncated Kir6.2 product, as the apparent molecular weight

shifted with addition of the C-terminal GFP tag. Based on the molecular weight, we predict that the truncated protein product initiated from a start codon in the first transmembrane domain. Therefore, we believe it is unlikely that this protein would form functional channels or traffic to the plasma membrane. When Kir6.2-W311^{TAG}-HA or Kir6.2-W311^{TAG}-HA-GFP were co-transfected with SUR1, pANAP, and eRF1-E55D, and cells were cultured in the presence of ANAP, the western blots were similar to wild-type Kir6.2-HA or Kir6.2-HA-GFP. Over 90% full-length Kir6.2*-HA-GFP was produced under these conditions (Figure 1—Figure supplement 1D). We were unable to quantify the percentage of full-length Kir6.2*-HA produced as the C-terminally truncated band resulting from termination at the TAG codon was very similar in size to the N-terminally truncated band. Co-expression with SUR1 increased the percentage of full-length Kir6.2*-HA-GFP produced (Figure 1—Figure supplement 1D). In the absence of ANAP, we did not observe any full-length Kir6.2, indicating that there was no read-through of the amber (TAG) stop codon (Figure 1—Figure supplement 1D).

528 Confocal microscopy.

Confocal imaging was performed using a spinning-disk system (Ultra-VIEW VoX, PerkinElmer; Waltham, MA) mounted on an IX81 microscope (Olympus; Southend-on-Sea, UK) with a Plan Apo 60x oil immersion objective (NA = 1.4), provided by the Micron Advanced Bioimaging Unit, Oxford. Transfected HEK-293T cells were incubated for 15 minutes with 1 nM CellMask Deep Red (Thermo Fisher) to stain plasma membranes before washing with PBS and imaging. ANAP was excited with a solid-state laser at 405 nM. GFP and CellMask were excited with an argon laser at 488 nM and 633 nM respectively. Images were captured on an EMCCD camera (ImagEM; Hamamatsu Photonics; Welwyn Garden City, UK) binned at 2 x 2 pixels and analysed using Python. A median filter with a box size of 32 x 32 pixels was applied to improve the signal-to-noise ratio by reducing background fluorescence.

We examined the surface expression of our ANAP-labelled constructs using confo-

541 cal microscopy (Figure 1—Figure supplement 1A,B). When Kir6.2-W311^{TAG}-GFP was co-
 542 transfected with SUR1 along with pANAP and eRF1-E55D in the presence of ANAP, the
 543 ANAP and GFP fluorescence were co-localized at the plasma membrane. When wild-type
 544 Kir6.2-GFP was transfected under the same conditions, only GFP fluorescence was ob-
 545 served at the plasma membrane. ANAP fluorescence was diffuse and confined to the
 546 cytoplasm or intracellular structures. Thus, the plasma-membrane ANAP signal was spe-
 547 cific for Kir6.2*-GFP.

548 **Surface expression assays.**

549 We measured surface expression of HA-tagged Kir6.2 subunits using an approach out-
 550 lined by Zerangue et al. (*Zerangue et al., 1999; Puljung et al., 2019*). Cells were plated
 551 on 19 mm coverslips coated with poly-l-lysine and transfected as described above. Fol-
 552 lowing incubation, cells were rinsed with PBS before fixation with 10% formalin for 30
 553 minutes at room temperature. After washing again, cells were blocked with 1% BSA in
 554 PBS for 30 minutes at 4 °C before a 1-hour incubation at 4 °C with a 1:1000 dilution (in
 555 PBS) of rat anti-HA monoclonal antibodies. Cells were then washed 5 times on ice with
 556 1% BSA in PBS followed by a 30-minute incubation at 4 °C with a 1:2000 dilution of HRP-
 557 conjugated goat anti-rat polyclonal antibodies. Cells were washed 5 times in PBS + 1%
 558 BSA and 4 times in PBS. Coverslips were removed from the culture dishes and placed in
 559 clean, untreated dishes for measurement. 300 µl of SuperSignal ELISA Femto Maximum
 560 Sensitivity Substrate (Thermo Fisher) was added to each sample and the luminescence
 561 was measured using a Glomax 20/20 Luminometer (Promega; Madison, WI) after a 10
 562 second incubation.

563 HEK-293T cells were transfected with Kir6.2 constructs with or without a TAG stop
 564 codon corresponding to position 311. Cells were co-transfected with pANAP and eRF1-
 565 E55D in the presence or absence of SUR1 and cultured with or without ANAP. Wild-type
 566 Kir6.2-HA and Kir6.2-HA-GFP in the presence of SUR1 were included as positive controls.
 567 Kir6.2 constructs with no HA tag served as negative controls. In the presence of ANAP,

568 we observed strong trafficking of Kir6.2*-HA-GFP to the plasma membrane, but much
 569 less trafficking of Kir6.2*-HA (Figure 1—Figure supplement 1E). When cells were cultured
 570 in the absence of ANAP, we observed little to no Kir6.2 surface expression from cells that
 571 were transfected with Kir6.2-W311^{TAG}-HA or Kir6.2-W311^{TAG}-HA-GFP, suggesting that pre-
 572 maturely truncated constructs did not traffic to the plasma membrane. In the absence
 573 of SUR1, surface expression was weak for both wild-type and tagged constructs, despite
 574 the reported ability of Kir6.2-GFP to traffic to the plasma membrane in the absence of
 575 SUR1 (*John et al., 1998; Makhina and Nichols, 1998*).

576 **Epifluorescence imaging and spectroscopy.**

577 Epifluorescence imaging and spectroscopy were performed using a Nikon Eclipse TE2000-
 578 U microscope with a 60x water immersion objective (Plan Apo VC, NA = 1.2, Nikon; Kingston
 579 upon Thames, UK) or a 100x oil immersion objective (Nikon, Apo TIRF, NA = 1.49). Imag-
 580 ing of ANAP was performed using a 385 nm LED source (ThorLabs; Newton, NJ) with a
 581 390/18 nm band-pass excitation filter, an MD416 dichroic and a 479/40 nm band-pass
 582 emission filter (all from ThorLabs). GFP was imaged using a 490 nm LED source (Thor-
 583 Labs) with a 480/40 nm band-pass excitation filter, a DM505 dichroic, and a 510 nm long-
 584 pass emission filter (all from Chroma; Bellows Falls, VT). Fluorescence spectra were col-
 585 lected by exciting ANAP as above but using a 400 nm long-pass emission filter (Thor-
 586 Labs), then passing emitted light through an IsoPlane 160 Spectrometer (Princeton In-
 587 struments; Trenton, NJ) with a 300 g mm⁻¹ grating. Images were collected with 0.1 s to
 588 1 s exposures on a Pixis 400BR_eXcelon CCD (Princeton Instruments).

589 **Electrophysiology.**

590 Patch pipettes were pulled from thick-walled borosilicate glass capillaries (GC150F-15,
 591 Harvard Apparatus; Holliston, MA) to a resistance of 1.5 MΩ to 2.5 MΩ when filled with
 592 pipette solution. Currents were recorded at -60 mV from excised inside-out patches
 593 using an Axopatch 200B amplifier equipped with a Digidata 1322A digitizer and using
 594 pClamp 10 software (Molecular Devices; San Jose, CA). Currents were low-pass filtered

595 at 5 kHz and digitized at 20 kHz. The bath solution (intracellular) contained 140 mM KCl,
596 10 mM HEPES, 1 mM EDTA and 1 mM EGTA (pH 7.3 with KOH). The pipette solution (ex-
597 tracellular) contained 140 mM KCl, 10 mM HEPES and 1 mM EDTA (pH 7.4 with KOH).
598 All experiments were carried out in Mg²⁺-free conditions. Currents were leak corrected
599 using the current remaining in bath solution containing 5 mM barium acetate at 60 mV,
600 assuming a linear leak with a reversal potential of 0 mV. Inhibition was calculated and
601 corrected for rundown by alternating test concentrations of nucleotide solution with
602 nucleotide-free solution, then expressing the test currents as a fraction of the average
603 of the control currents before and after the test solution as described previously (*Proks*
604 *et al., 2010*).

605 **Unroofed binding measurements.**

606 Unroofed membranes were prepared as described previously (*Heuser, 2000; Zagotta*
607 *et al., 2016; Puljung et al., 2019*). A coverslip plated with transfected HEK-293T cells was
608 removed from the culture media and rinsed with PBS. The coverslip was then briefly son-
609 icated using a probe sonicator (Vibra-cell; Newtown, CT) leaving behind adherent plasma
610 membrane fragments. Cells cultured on FluoroDishes were rinsed and sonicated directly
611 in the dish. Unroofed membrane fragments were nearly invisible in bright-field images
612 and identified by their GFP and ANAP fluorescence. Fluorescent TNP-nucleotides (Jena
613 Bioscience; Jena, Germany) were diluted in bath solution and perfused onto unroofed
614 membranes using a valve controlled microvolume superfusion system (μFlow, ALA Sci-
615 entific Instruments; Farmingdale, NY).

616 Fluorescence spectra were collected as described above. A region of interest corre-
617 sponding to the membrane fragment was manually selected and line-averaged for each
618 wavelength. A similarly sized region of background was selected and averaged, then
619 subtracted from the spectrum of interest. After subtraction, ANAP intensity was calcu-
620 lated by averaging the fluorescence intensity measured between 469.5 nm and 474.5 nm.
621 Bleaching was corrected by fitting the normalised ANAP intensity of exposures taken dur-

622 ing perfusion with nucleotide-free solution to a single exponential decay of the form

$$\frac{F}{F_{max}} = ae^{kt} + (1 - a) \quad (1)$$

623 then using the fit to correct the intensity of exposures taken during perfusion with test
624 nucleotide solutions.

625 For kinetic measurements, the solution changer and camera were controlled using
626 pClamp 10 software coupled to a Digidata 1322A digitizer. Each fragment of unroofed
627 membrane was exposed three times to the same test concentration of nucleotide. Spec-
628 tra were acquired every three seconds. These technical replicates were averaged and
629 presented as a single experiment. Bleaching was corrected by fitting the ANAP intensity
630 of the last ten spectra acquired during each nucleotide-free solution wash to equation 1.

631 Some experiments were excluded from further analysis due to obvious cross-contamination
632 between different solutions within the μ Flow superfusion system. These were identified
633 by noticeable colour changes in the solution in the delivery tubes.

634 Patch-clamp fluorometry.

635 The tip of the patch pipette was centred on the slit of the spectrometer immediately after
636 patch excision. Currents were measured as described above. Fluorescence emission
637 spectra from the excised patch were acquired concurrently with current measurements,
638 both during test solution application as well as nucleotide-free solution. Background
639 subtraction was slightly imperfect due to the exclusion of TNP-ATP from volume of the
640 glass of the pipette, resulting in spectra that have negative intensities at the TNP-ATP
641 peak at high nucleotide concentrations. However, this over-subtraction does not affect
642 the size of the ANAP peak, which we used to quantify nucleotide binding.

643 Some experiments were excluded from further analysis due to low fluorescence in-
644 tensity, as we were concerned about a low signal to noise ratio influencing our results.

645 **Data processing and presentation.**

646 Raw spectrographic images and current traces were pre-processed in Python and Clamp-
 647 fit (Axon) before analysis with R. Where applicable, all experimental data points are dis-
 648 played in each figure. The number of experiments is reported in the figure legends and
 649 tables. To help visualise uncertainty and prevent some data points being hidden, they are
 650 arranged with a small amount of horizontal jitter; vertical position remains unaffected.
 651 Unless otherwise stated, summary statistics are overlaid as the mean with error bars rep-
 652 resenting the standard error of the mean. Where these error bars are not visible, they
 653 are smaller than the size of the point used for the mean.

654 Hill fits to fluorescence quenching were nonlinear least-squares fits to the following
 655 equation:

$$\frac{y}{y_{max}} = E_{max} + \frac{1 - E_{max}}{1 + 10^{(EC_{50} - [TNPATP]) \cdot h}} \quad (2)$$

656 where y represents normalised fluorescence intensity and EC_{50} and $[TNPATP]$ are \log_{10}
 657 values. Current inhibition data were fit to the same equation but with y representing
 658 normalised current magnitude, IC_{50} instead of EC_{50} , and I_{max} instead of E_{max} .

659 k_{obs} values from single exponential fits with equation 1 to the wash-on and wash-off
 660 of TNP-ATP in the time-course experiments were fit with the linear equation:

$$k_{obs} = k_{on}[TNPATP] + k_{off} \quad (3)$$

661 The gradient of the linear fit to the observed on-rate (k_{obs}) is equivalent to k_{on} ; k_{off} is the
 662 intercept at zero $[TNPATP]$. We also measured k_{off} directly from the dequenching of
 663 ANAP following TNP-ATP wash-off. As expected, these values were independent of the
 664 $[TNPATP]$ applied.

665 **Bayesian model fitting.**

666 The MWC-type models considered (Figure 2 and Figure 2—Figure Supplement 2) were
 667 formulated as follows:

$$\frac{F}{F_{max}} = \frac{K_A[TNPATP](1+K_A[TNPATP])^3 + LDK_A[TNPATP](1+DK_A[TNPATP])^3}{(1+K_A[TNPATP])^4 + L(1+DK_A[TNPATP])^4} \quad (4)$$

$$\frac{\text{open channels}}{\text{total channels}} = \frac{L(1+DK_A[TNPATP])^4}{(1+K_A[TNPATP])^4 + L(1+DK_A[TNPATP])^4} \quad (5)$$

668 When no ligand is present (i.e. when $[TNPATP] = 0$), equation 5 becomes:

$$\frac{\text{open channels}}{\text{total channels}} = \frac{L}{1+L} \quad (6)$$

669 We can use this to normalise the predicted changes in the open fraction to an ob-
 670 served change in current as:

$$\frac{I}{I_{max}} = \frac{L(1+DK_A[TNPATP])^4}{(1+K_A[TNPATP])^4 + L(1+DK_A[TNPATP])^4} \cdot \frac{1+L}{L} \quad (7)$$

671 Two variations on the full MWC model were also considered, and diagrammatic for-
 672 mulations are shown in Figure 2 - Figure supplement 1. The first was similar to the MWC-
 673 type model, except that the channels close after one molecule of TNP-ATP binding with
 674 subsequent binding events having no effect.

$$\frac{F}{F_{max}} = \frac{LDK_A[TNPATP](1+3K_A[TNPATP]+3K_A^2[TNPATP]^2 + K_A^3[TNPATP]^3) + K_A[TNPATP](1+K_A[TNPATP])^3}{L(1+4DK_A[TNPATP]+6DK_A^2[TNPATP]^2+4DK_A^3[TNPATP]^3 + DK_A^4[TNPATP]^4) + (1+K_A[TNPATP])^4} \quad (8)$$

$$\frac{I}{I_{max}} = \frac{L(1+4DK_A[TNPATP]+6DK_A^2[TNPATP]^2+4DK_A^3[TNPATP]^3 + DK_A^4[TNPATP]^4)}{L(1+4DK_A[TNPATP]+6DK_A^2[TNPATP]^2+4DK_A^3[TNPATP]^3 + DK_A^4[TNPATP]^4) + (1+K_A[TNPATP])^4} \cdot \frac{1+L}{L} \quad (9)$$

675 The second alternate model was the same as the full MWC model, but with an addi-

676 tional term C describing binding cooperativity between Kir6.2 subunits.

$$\frac{F}{F_{max}} = \frac{LDK_A[TNPATP](1 + 3CDK_A[TNPATP] + 3C^2D^2K_A^2[TNPATP]^2 + C^3D^3K_A^3[TNPATP]^3) + K_A[TNPATP](1 + 3CK_A[TNPATP] + 3C^2K_A^2[TNPATP]^2 + C^3K_A^3[TNPATP]^3)}{L(1 + 4DK_A[TNPATP] + 6CD^2K_A^2[TNPATP]^2 + 4C^2D^3K_A^3[TNPATP]^3 + C^3D^4K_A^4[TNPATP]^4) + 1 + 4K_A[TNPATP] + 6CK_A^2[TNPATP]^2 + 4C^2K_A^3[TNPATP]^3 + C^3K_A^4[TNPATP]^4} \quad (10)$$

$$\frac{I}{I_{max}} = \frac{L(1 + 4DK_A[TNPATP] + 6CD^2K_A^2[TNPATP]^2 + 4C^2D^3K_A^3[TNPATP]^3 + C^3D^4K_A^4[TNPATP]^4)}{L(1 + 4DK_A[TNPATP] + 6CD^2K_A^2[TNPATP]^2 + 4C^2D^3K_A^3[TNPATP]^3 + C^3D^4K_A^4[TNPATP]^4) + 1 + 4K_A[TNPATP] + 6CK_A^2[TNPATP]^2 + 4C^2K_A^3[TNPATP]^3 + C^3K_A^4[TNPATP]^4} \cdot \frac{1+L}{L} \quad (11)$$

677 Each model was fit to the combined patch-clamp fluorometry datasets using the brms
 678 package (*Gelman et al., 2015; Burkner, 2017*) in R. Prior probability distributions for each
 679 parameter were supplied as:

$$\log_{10}(L) \sim Normal(\mu : 0, \sigma^2 : 0.7)$$

$$D \sim Uniform(min : 0, max : 1)$$

$$\log_{10}(K_A) \sim Uniform(min : 2, max : 6)$$

$$C \sim Uniform(min : 0, max : 1)$$

680 so that all priors are flat apart from L, which is weakly informative with 99% of its density
 681 falling between unliganded open probabilities of 0.01 and 0.99, and 85% falling between
 682 0.1 and 0.9.

683 Each model was run with 4 independent chains for 10,000 iterations each after a burn-
 684 in period of 20,000 iterations, saving every 10th sample for a total of 4,000 samples per
 685 model. Each model parameter achieved a minimum effective sample size of 3,500 and
 686 a potential scale reduction statistic (\hat{R}) of 1.00. Where applicable, the posterior proba-
 687 bilities of each parameter are reported as the median and the 95% equal-tailed interval.
 688 Bayes factors were calculated using bridge-sampling (*Gronau et al., 2017*), and leave-one-
 689 out cross-validation (LOO-CV) was performed using the loo package (*Vehtari et al., 2017*).

690 **Docking.**

691 Computational docking of TNP-ATP into the nucleotide binding site of Kir6.2 was per-
 692 formed using AutoDock-Vina (*Trott and Olson, 2010*) and Pymol (Schrödinger, LLC; New
 693 York, NY). 11 TNP-ATP structures from the Protein Data Bank (PDB accession #s 1I5D,
 694 3AR7, 5NCQ, 5SVQ, 5XW6, 2GVD, 5A3S, 2PMK, and 3B5J) were used as starting poses and
 695 a 15x11.25x15 Å box was centred on the ATP bound to Kir6.2 in PDB accession #6BAA
 696 (*Martin et al., 2017*). Protonation states for each residue were assigned using PDB2PQR
 697 and PROPKA 3.0 (*Dolinsky et al., 2004*). The modal highest-scoring pose from the dock-
 698 ing run was selected (PDB accession #5XW6, *Kasuya et al. (2017)*) and distances were
 699 measured from a pseudo atom at the centre of the fluorescent moiety. TNP-ATP (PDB
 700 #3AR7, *Toyoshima et al. (2011)*) was positioned into the first nucleotide binding domain
 701 of SUR1 (PDB #6PZI, *Martin et al. (2019)*) using the alignment tool in Pymol.

702 **Chemicals and stock solutions.**

703 Unless otherwise noted, all chemicals were obtained from Sigma. TNP-ATP was obtained
 704 as a 10 mM aqueous stock from Jena Bioscience and stored at –20 °C. 1 mM aqueous
 705 stocks of ANAP-TFA were prepared by dissolving the free acid in 30 mM NaOH, and were
 706 stored at –20 °C. Tolbutamide stocks (50 mM) were prepared in 100 mM KOH and stored
 707 at –20 °C.

708 **Data availability**

709 All data sets and the code used to analyse and present them are available on GitHub at
 710 https://github.com/smusher/KATP_paper_2019 and have also been uploaded to Dryad
 711 at <https://doi.org/10.5061/dryad.0vt4b8gtv>.

712 **Acknowledgments**

713 We wish to thank Raul Terron Exposito for technical assistance and Dr. Natascia Vedovato
 714 for helpful discussions. James Cantley provided access to the Licor scanner for western

715 blots. This work was supported by the Biotechnology and Biological Science Research
 716 Council (BB/R002517/1) and the Wellcome Trust Oxion graduate program.

717 References

- 718 **Aguilar-Bryan L**, Nichols CG, Wechsler SW, Clement JP, Boyd r A E, Gonzalez G, Herrera-Sosa H,
 719 Nguy K, Bryan J, Nelson DA. Cloning of the beta cell high-affinity sulfonylurea receptor: a reg-
 720 ulator of insulin secretion. *Science*. 1995; 268(5209):423–6. [HTTPS://WWW.NCBI.NLM.NIH.GOV/](https://www.ncbi.nlm.nih.gov/)
 721 [PUBMED/7716547](#).
- 722 **Ashcroft FM**, Puljung MC, Vedovato N. Neonatal Diabetes and the KATP Channel: From Mutation
 723 to Therapy. *Trends Endocrinol Metab*. 2017; 28(5):377–387. [HTTPS://WWW.NCBI.NLM.NIH.GOV/](https://www.ncbi.nlm.nih.gov/)
 724 [PUBMED/28262438](#), doi: [10.1016/j.tem.2017.02.003](https://doi.org/10.1016/j.tem.2017.02.003).
- 725 **Ashcroft FM**, Rorsman P. K(ATP) channels and islet hormone secretion: new insights and con-
 726 troversies. *Nat Rev Endocrinol*. 2013; 9(11):660–9. [HTTPS://WWW.NCBI.NLM.NIH.GOV/PUBMED/](https://www.ncbi.nlm.nih.gov/)
 727 [24042324](#), doi: [10.1038/nrendo.2013.166](https://doi.org/10.1038/nrendo.2013.166).
- 728 **Babenko AP**, Bryan J. Sur domains that associate with and gate KATP pores define a novel
 729 gatekeeper. *J Biol Chem*. 2003; 278(43):41577–80. [HTTPS://WWW.NCBI.NLM.NIH.GOV/PUBMED/](https://www.ncbi.nlm.nih.gov/)
 730 [12941953](#), doi: [10.1074/jbc.C300363200](https://doi.org/10.1074/jbc.C300363200).
- 731 **Biskup C**, Kusch J, Schulz E, Nache V, Schwede F, Lehmann F, Hagen V, Benndorf K. Relating ligand
 732 binding to activation gating in CNGA2 channels. *Nature*. 2007; 446(7134):440–3. [HTTPS://WWW.NCBI.NLM.NIH.GOV/PUBMED/17322905](https://www.ncbi.nlm.nih.gov/), doi: [10.1038/nature05596](https://doi.org/10.1038/nature05596).
- 734 **Burkner PC**. brms: An R Package for Bayesian Multilevel Models Using Stan. *Journal of Statistical*
 735 *Software*. 2017; 80(1):1–28. <GotoISI>[://WOS:000408409900001](https://wos:000408409900001).
- 736 **Chan KW**, Zhang H, Logothetis DE. N-terminal transmembrane domain of the SUR controls traf-
 737 ficking and gating of Kir6 channel subunits. *EMBO J*. 2003; 22(15):3833–43. [HTTPS://WWW.NCBI.NLM.NIH.GOV/PUBMED/12881418](https://www.ncbi.nlm.nih.gov/), doi: [10.1093/emboj/cdg376](https://doi.org/10.1093/emboj/cdg376).
- 739 **Chatterjee A**, Guo J, Lee HS, Schultz PG. A genetically encoded fluorescent probe in mam-
 740 malian cells. *J Am Chem Soc*. 2013; 135(34):12540–3. [HTTPS://WWW.NCBI.NLM.NIH.GOV/PUBMED/](https://www.ncbi.nlm.nih.gov/)
 741 [23924161](#), doi: [10.1021/ja4059553](https://doi.org/10.1021/ja4059553).

- 742 **Craig TJ**, Ashcroft FM, Proks P. How ATP inhibits the open K(ATP) channel. *J Gen
743 Physiol.* 2008; 132(1):131–44. [HTTPS://WWW.NCBI.NLM.NIH.GOV/PUBMED/18591420](https://www.ncbi.nlm.nih.gov/pmc/articles/PMC18591420/), doi:
744 [10.1085/jgp.200709874](https://doi.org/10.1085/jgp.200709874).
- 745 **Ding D**, Wang M, Wu JX, Kang Y, Chen L. The Structural Basis for the Binding of Repaglinide to
746 the Pancreatic KATP Channel. *Cell Rep.* 2019; 27(6):1848–1857 e4. [HTTPS://WWW.NCBI.NLM.NIH.GOV/PUBMED/31067468](https://www.ncbi.nlm.nih.
747 gov/pmc/articles/PMC31067468/), doi: [10.1016/j.celrep.2019.04.050](https://doi.org/10.1016/j.celrep.2019.04.050).
- 748 **Dolinsky TJ**, Nielsen JE, McCammon JA, Baker NA. PDB2PQR: an automated pipeline for the
749 setup of Poisson-Boltzmann electrostatics calculations. *Nucleic Acids Res.* 2004; 32(Web Server
750 issue):W665–7. [HTTPS://WWW.NCBI.NLM.NIH.GOV/PUBMED/15215472](https://www.ncbi.nlm.nih.gov/pmc/articles/PMC15215472/), doi: [10.1093/nar/gkh381](https://doi.org/10.1093/nar/gkh381).
- 751 **Drain P**, Geng X, Li L. Concerted gating mechanism underlying KATP channel inhibition by
752 ATP. *Biophys J.* 2004; 86(4):2101–12. [HTTPS://WWW.NCBI.NLM.NIH.GOV/PUBMED/15041650](https://www.ncbi.nlm.nih.gov/pmc/articles/PMC15041650/), doi:
753 [10.1016/S0006-3495\(04\)74269-1](https://doi.org/10.1016/S0006-3495(04)74269-1).
- 754 **Drain P**, Li L, Wang J. KATP channel inhibition by ATP requires distinct functional domains of the cy-
755 toplasmic C terminus of the pore-forming subunit. *Proc Natl Acad Sci U S A.* 1998; 95(23):13953–8.
756 [HTTPS://WWW.NCBI.NLM.NIH.GOV/PUBMED/9811907](https://www.ncbi.nlm.nih.gov/pmc/articles/PMC18591420/).
- 757 **Enkvetachakul D**, Loussouarn G, Makhina E, Shyng SL, Nichols CG. The kinetic and physical basis of
758 K(ATP) channel gating: toward a unified molecular understanding. *Biophys J.* 2000; 78(5):2334–
759 48. [HTTPS://WWW.NCBI.NLM.NIH.GOV/PUBMED/10777731](https://www.ncbi.nlm.nih.gov/pmc/articles/PMC18591420/), doi: [10.1016/S0006-3495\(00\)76779-8](https://doi.org/10.1016/S0006-3495(00)76779-8).
- 760 **Enkvetachakul D**, Nichols CG. Gating mechanism of KATP channels: function fits form. *J
761 Gen Physiol.* 2003; 122(5):471–80. [HTTPS://WWW.NCBI.NLM.NIH.GOV/PUBMED/14581579](https://www.ncbi.nlm.nih.gov/pmc/articles/PMC18591420/), doi:
762 [10.1085/jgp.200308878](https://doi.org/10.1085/jgp.200308878).
- 763 **Fang K**, Csanady L, Chan KW. The N-terminal transmembrane domain (TMD0) and a cytoso-
764 lic linker (L0) of sulphonylurea receptor define the unique intrinsic gating of KATP channels.
765 *J Physiol.* 2006; 576(Pt 2):379–89. [HTTPS://WWW.NCBI.NLM.NIH.GOV/PUBMED/16887879](https://www.ncbi.nlm.nih.gov/pmc/articles/PMC18591420/), doi:
766 [10.1113/jphysiol.2006.112748](https://doi.org/10.1113/jphysiol.2006.112748).
- 767 **Flanagan SE**, Edghill EL, Gloyn AL, Ellard S, Hattersley AT. Mutations in KCNJ11, which encodes
768 Kir6.2, are a common cause of diabetes diagnosed in the first 6 months of life, with the pheno-

- 769 type determined by genotype. *Diabetologia*. 2006; 49(6):1190–7. [HTTPS://WWW.NCBI.NLM.NIH.GOV/PUBMED/16609879](https://www.ncbi.nlm.nih.gov/pmc/articles/PMC16609879/), doi: 10.1007/s00125-006-0246-z.
- 770
771 **Gelman A**, Lee D, Guo JQ. Stan: A Probabilistic Programming Language for Bayesian Infer-
772 ence and Optimization. *Journal of Educational and Behavioral Statistics*. 2015; 40(5):530–543.
773 <[Goto ISI](https://doi.org/10.1080/000363883900006)>://WOS:000363883900006.
- 774 **Gloyn AL**, Diatloff-Zito C, Edghill EL, Bellanne-Chantelot C, Nivot S, Coutant R, Ellard S, Hattersley AT,
775 Robert JJ. KCNJ11 activating mutations are associated with developmental delay, epilepsy and
776 neonatal diabetes syndrome and other neurological features. *Eur J Hum Genet*. 2006; 14(7):824–
777 30. [HTTPS://WWW.NCBI.NLM.NIH.GOV/PUBMED/16670688](https://www.ncbi.nlm.nih.gov/pmc/articles/PMC16670688/), doi: 10.1038/sj.ejhg.5201629.
- 778 **Gribble FM**, Tucker SJ, Haug T, Ashcroft FM. MgATP activates the beta cell KATP channel by
779 interaction with its SUR1 subunit. *Proc Natl Acad Sci U S A*. 1998; 95(12):7185–90. [HTTPS://WWW.NCBI.NLM.NIH.GOV/PUBMED/9618560](https://www.ncbi.nlm.nih.gov/pmc/articles/PMC9618560/), doi: 10.1073/pnas.95.12.7185.
- 780
781 **Gronau QF**, Singmann H, Wagenmakers EJ. bridgesampling: An R Package for Estimating Normal-
782 izing Constants. *arXiv e-prints*. 2017 Oct; p. arXiv:1710.08162.
- 783 **Heuser J**. The production of 'cell cortices' for light and electron microscopy. *Traffic*. 2000; 1(7):545–
784 52. [HTTPS://WWW.NCBI.NLM.NIH.GOV/PUBMED/11208142](https://www.ncbi.nlm.nih.gov/pmc/articles/PMC11208142/).
- 785 **Hines KE**, Middendorf TR, Aldrich RW. Determination of parameter identifiability in nonlinear bio-
786 physical models: A Bayesian approach. *J Gen Physiol*. 2014; 143(3):401–16. [HTTPS://WWW.NCBI.NLM.NIH.GOV/PUBMED/24516188](https://www.ncbi.nlm.nih.gov/pmc/articles/PMC4516188/), doi: 10.1085/jgp.201311116.
- 787
788 **Inagaki N**, Gono T, Clement JP, Namba N, Inazawa J, Gonzalez G, Aguilar-Bryan L, Seino S, Bryan
789 J. Reconstitution of IKATP: an inward rectifier subunit plus the sulfonylurea receptor. *Science*.
790 1995; 270(5239):1166–70. [HTTPS://WWW.NCBI.NLM.NIH.GOV/PUBMED/7502040](https://www.ncbi.nlm.nih.gov/pmc/articles/PMC7502040/).
- 791 **Inagaki N**, Gono T, Seino S. Subunit stoichiometry of the pancreatic beta-cell ATP-sensitive K+
792 channel. *FEBS Lett*. 1997; 409(2):232–6. [HTTPS://WWW.NCBI.NLM.NIH.GOV/PUBMED/9202152](https://www.ncbi.nlm.nih.gov/pmc/articles/PMC9202152/).
- 793 **John SA**, Monck JR, Weiss JN, Ribalet B. The sulphonylurea receptor SUR1 regulates ATP-sensitive
794 mouse Kir6.2 K+ channels linked to the green fluorescent protein in human embryonic kidney
795 cells (HEK 293). *J Physiol*. 1998; 510 (Pt 2):333–45. [HTTPS://WWW.NCBI.NLM.NIH.GOV/PUBMED/9705987](https://www.ncbi.nlm.nih.gov/pmc/articles/PMC9705987/), doi: 10.1111/j.1469-7793.1998.333bk.x.
- 796

- 797 **Kasuya G**, Yamaura T, Ma XB, Nakamura R, Takemoto M, Nagumo H, Tanaka E, Dohmae N, Nakane
 798 T, Yu Y, Ishitani R, Matsuzaki O, Hattori M, Nureki O. Structural insights into the competitive
 799 inhibition of the ATP-gated P2X receptor channel. *Nat Commun.* 2017; 8(1):876. [HTTPS://WWW.NCBI.NLM.NIH.GOV/PUBMED/29026074](https://www.ncbi.nlm.nih.gov/pmc/articles/PMC546074/), doi: 10.1038/s41467-017-00887-9.
- 800
- 801 **Kusch J**, Biskup C, Thon S, Schulz E, Nache V, Zimmer T, Schwede F, Benndorf K. Interdependence of
 802 receptor activation and ligand binding in HCN2 pacemaker channels. *Neuron*. 2010; 67(1):75–85.
 803 [HTTPS://WWW.NCBI.NLM.NIH.GOV/PUBMED/20624593](https://www.ncbi.nlm.nih.gov/pmc/articles/PMC2862459/), doi: 10.1016/j.neuron.2010.05.022.
- 804 **Li L**, Wang J, Drain P. The I182 region of k(ir)6.2 is closely associated with ligand binding in K(ATP)
 805 channel inhibition by ATP. *Biophys J.* 2000; 79(2):841–52. [HTTPS://WWW.NCBI.NLM.NIH.GOV/PUBMED/10920016](https://www.ncbi.nlm.nih.gov/pmc/articles/PMC10920016/), doi: 10.1016/S0006-3495(00)76340-5.
- 806
- 807 **Lin CY**, Huang Z, Wen W, Wu A, Wang C, Niu L. Enhancing Protein Expression in HEK-293 Cells by
 808 Lowering Culture Temperature. *PLoS One*. 2015; 10(4):e0123562. [HTTPS://WWW.NCBI.NLM.NIH.GOV/PUBMED/25893827](https://www.ncbi.nlm.nih.gov/pmc/articles/PMC45893827/), doi: 10.1371/journal.pone.0123562.
- 809
- 810 **Makhina EN**, Nichols CG. Independent trafficking of KATP channel subunits to the plasma mem-
 811 brane. *J Biol Chem.* 1998; 273(6):3369–74. [HTTPS://WWW.NCBI.NLM.NIH.GOV/PUBMED/9452456](https://www.ncbi.nlm.nih.gov/pmc/articles/PMC9452456/).
- 811
- 812 **Markworth E**, Schwanstecher C, Schwanstecher M. ATP4- mediates closure of pancreatic beta-
 813 cell ATP-sensitive potassium channels by interaction with 1 of 4 identical sites. *Diabetes*.
 814 2000; 49(9):1413–8. [HTTPS://WWW.NCBI.NLM.NIH.GOV/PUBMED/10969823](https://www.ncbi.nlm.nih.gov/pmc/articles/PMC10969823/), doi: 10.2337/dia-
 815 betes.49.9.1413.
- 816
- 816 **Martin GM**, Kandasamy B, DiMaio F, Yoshioka C, Shyng SL. Anti-diabetic drug binding site in a
 817 mammalian KATP channel revealed by Cryo-EM. *Elife*. 2017; 6. [HTTPS://WWW.NCBI.NLM.NIH.GOV/PUBMED/29035201](https://www.ncbi.nlm.nih.gov/pmc/articles/PMC29035201/), doi: 10.7554/eLife.31054.
- 818
- 819 **Martin GM**, Sung MW, Yang Z, Innes LM, Kandasamy B, David LL, Yoshioka C, Shyng SL. Mechanism
 820 of pharmacochaperoning in a mammalian KATP channel revealed by cryo-EM. *Elife*. 2019; 8.
 821 [HTTPS://WWW.NCBI.NLM.NIH.GOV/PUBMED/31343405](https://www.ncbi.nlm.nih.gov/pmc/articles/PMC31343405/), doi: 10.7554/eLife.46417.
- 822
- 822 **Masia R**, Koster JC, Tumini S, Chiarelli F, Colombo C, Nichols CG, Barbetti F. An ATP-binding mu-
 823 tation (G334D) in KCNJ11 is associated with a sulfonylurea-insensitive form of developmental

- 824 delay, epilepsy, and neonatal diabetes. *Diabetes*. 2007; 56(2):328–36. [HTTPS://WWW.NCBI.NLM.NIH.GOV/PUBMED/17259376](https://www.ncbi.nlm.nih.gov/pmc/articles/PMC17259376/), doi: 10.2337/db06-1275.
- 825
- 826 **McTaggart JS**, Clark RH, Ashcroft FM. The role of the KATP channel in glucose homeostasis in health
827 and disease: more than meets the islet. *J Physiol.* 2010; 588(Pt 17):3201–9. [HTTPS://WWW.NCBI.NLM.NIH.GOV/PUBMED/20519313](https://www.ncbi.nlm.nih.gov/pmc/articles/PMC20519313/), doi: 10.1113/jphysiol.2010.191767.
- 828
- 829 **Monod J**, Wyman J, Changeux JP. On the Nature of Allosteric Transitions: A Plausible Model. *J Mol
830 Biol.* 1965; 12:88–118. [HTTPS://WWW.NCBI.NLM.NIH.GOV/PUBMED/14343300](https://www.ncbi.nlm.nih.gov/pmc/articles/PMC14343300/).
- 831
- 832 **Nichols CG**, Shyng SL, Nestorowicz A, Glaser B, Clement JP, Gonzalez G, Aguilar-Bryan L, Permutt
833 MA, Bryan J. Adenosine diphosphate as an intracellular regulator of insulin secretion. *Science*.
1996; 272(5269):1785–7. [HTTPS://WWW.NCBI.NLM.NIH.GOV/PUBMED/8650576](https://www.ncbi.nlm.nih.gov/pmc/articles/PMC8650576/).
- 834
- 835 **Pratt EB**, Zhou Q, Gay JW, Shyng SL. Engineered interaction between SUR1 and Kir6.2 that enhances
836 ATP sensitivity in KATP channels. *J Gen Physiol.* 2012; 140(2):175–87. [HTTPS://WWW.NCBI.NLM.NIH.GOV/PUBMED/22802363](https://www.ncbi.nlm.nih.gov/pmc/articles/PMC22802363/), doi: 10.1085/jgp.201210803.
- 837
- 838 **Proks P**, Puljung MC, Vedovato N, Sachse G, Mulvaney R, Ashcroft FM. Running out of time:
the decline of channel activity and nucleotide activation in adenosine triphosphate-sensitive K-
839 channels. *Philos Trans R Soc Lond B Biol Sci.* 2016; 371(1700). [HTTPS://WWW.NCBI.NLM.NIH.GOV/PUBMED/27377720](https://www.ncbi.nlm.nih.gov/pmc/articles/PMC27377720/), doi: 10.1098/rstb.2015.0426.
- 840
- 841 **Proks P**, de Wet H, Ashcroft FM. Activation of the K(ATP) channel by Mg-nucleotide interaction
842 with SUR1. *J Gen Physiol.* 2010; 136(4):389–405. [HTTPS://WWW.NCBI.NLM.NIH.GOV/PUBMED/20876358](https://www.ncbi.nlm.nih.gov/pmc/articles/PMC20876358/), doi: 10.1085/jgp.201010475.
- 843
- 844 **Puljung M**, Vedovato N, Usher S, Ashcroft F. Activation mechanism of ATP-sensitive K(+) channels
845 explored with real-time nucleotide binding. *Elife*. 2019; 8. [HTTPS://WWW.NCBI.NLM.NIH.GOV/PUBMED/30789344](https://www.ncbi.nlm.nih.gov/pmc/articles/PMC30789344/), doi: 10.7554/eLife.41103.
- 846
- 847 **Puljung MC**. Cryo-electron microscopy structures and progress toward a dynamic understand-
848 ing of KATP channels. *J Gen Physiol.* 2018; 150(5):653–669. [HTTPS://WWW.NCBI.NLM.NIH.GOV/PUBMED/29685928](https://www.ncbi.nlm.nih.gov/pmc/articles/PMC29685928/), doi: 10.1085/jgp.201711978.
- 849
- 850 **Quan Y**, Barszczyk A, Feng ZP, Sun HS. Current understanding of K ATP channels in neonatal

- 851 diseases: focus on insulin secretion disorders. *Acta Pharmacol Sin.* 2011; 32(6):765–80. [HTTPS://WWW.NCBI.NLM.NIH.GOV/PUBMED/21602835](https://www.ncbi.nlm.nih.gov/pmc/articles/PMC3147033/), doi: 10.1038/aps.2011.57.
- 852
- 853 **Ribalet B**, John SA, Xie LH, Weiss JN. ATP-sensitive K⁺ channels: regulation of bursting by the
854 sulphonylurea receptor, PIP2 and regions of Kir6.2. *J Physiol.* 2006; 571(Pt 2):303–17. [HTTPS://WWW.NCBI.NLM.NIH.GOV/PUBMED/16373383](https://www.ncbi.nlm.nih.gov/pmc/articles/PMC1453383/), doi: 10.1113/jphysiol.2005.100719.
- 855
- 856 **Sakura H**, Ammala C, Smith PA, Gribble FM, Ashcroft FM. Cloning and functional expression of
857 the cDNA encoding a novel ATP-sensitive potassium channel subunit expressed in pancreatic
858 beta-cells, brain, heart and skeletal muscle. *FEBS Lett.* 1995; 377(3):338–44. [HTTPS://WWW.NCBI.NLM.NIH.GOV/PUBMED/8549751](https://www.ncbi.nlm.nih.gov/pmc/articles/PMC8549751/), doi: 10.1016/0014-5793(95)01369-5.
- 859
- 860 **Schmied WH**, Elsasser SJ, Uttamapinant C, Chin JW. Efficient multisite unnatural amino acid in-
861 corporation in mammalian cells via optimized pyrrolysyl tRNA synthetase/tRNA expression and
862 engineered eRF1. *J Am Chem Soc.* 2014; 136(44):15577–83. [HTTPS://WWW.NCBI.NLM.NIH.GOV/PUBMED/25350841](https://www.ncbi.nlm.nih.gov/pmc/articles/PMC420841/), doi: 10.1021/ja5069728.
- 863
- 864 **Snider KE**, Becker S, Boyajian L, Shyng SL, MacMullen C, Hughes N, Ganapathy K, Bhatti T, Stan-
865 ley CA, Ganguly A. Genotype and phenotype correlations in 417 children with congenital hy-
866 perinsulinism. *J Clin Endocrinol Metab.* 2013; 98(2):E355–63. [HTTPS://WWW.NCBI.NLM.NIH.GOV/PUBMED/23275527](https://www.ncbi.nlm.nih.gov/pmc/articles/PMC3275527/), doi: 10.1210/jc.2012-2169.
- 867
- 868 **Toyoshima C**, Yonekura S, Tsueda J, Iwasawa S. Trinitrophenyl derivatives bind differently
869 from parent adenine nucleotides to Ca²⁺-ATPase in the absence of Ca²⁺. *Proc Natl Acad
870 Sci U S A.* 2011; 108(5):1833–8. [HTTPS://WWW.NCBI.NLM.NIH.GOV/PUBMED/21239683](https://www.ncbi.nlm.nih.gov/pmc/articles/PMC3147033/), doi:
871 10.1073/pnas.1017659108.
- 872
- 873 **Trapp S**, Proks P, Tucker SJ, Ashcroft FM. Molecular analysis of ATP-sensitive K channel gating and
874 implications for channel inhibition by ATP. *J Gen Physiol.* 1998; 112(3):333–49. [HTTPS://WWW.NCBI.NLM.NIH.GOV/PUBMED/9725893](https://www.ncbi.nlm.nih.gov/pmc/articles/PMC9725893/), doi: 10.1085/jgp.112.3.333.
- 875
- 876 **Trott O**, Olson AJ. AutoDock Vina: improving the speed and accuracy of docking with a new scoring
877 function, efficient optimization, and multithreading. *J Comput Chem.* 2010 Jan; 31(2):455–461.
- 878
- 879 **Tucker SJ**, Gribble FM, Zhao C, Trapp S, Ashcroft FM. Truncation of Kir6.2 produces ATP-sensitive

- 878 K⁺ channels in the absence of the sulphonylurea receptor. *Nature*. 1997; 387(6629):179–83.
- 879 [HTTPS://WWW.NCBI.NLM.NIH.GOV/PUBMED/9144288](https://www.ncbi.nlm.nih.gov/PUBMED/9144288), doi: 10.1038/387179a0.
- 880 **Tusnady GE**, Bakos E, Varadi A, Sarkadi B. Membrane topology distinguishes a subfamily of the
881 ATP-binding cassette (ABC) transporters. *FEBS Lett*. 1997; 402(1):1–3. [HTTPS://WWW.NCBI.NLM.NIH.GOV/PUBMED/9013845](https://www.ncbi.nlm.nih.gov/PUBMED/9013845), doi: 10.1016/s0014-5793(96)01478-0.
- 882
- 883 **Ueda K**, Komine J, Matsuo M, Seino S, Amachi T. Cooperative binding of ATP and MgADP in the
884 sulfonylurea receptor is modulated by glibenclamide. *Proc Natl Acad Sci U S A*. 1999; 96(4):1268–
885 72. [HTTPS://WWW.NCBI.NLM.NIH.GOV/PUBMED/9990013](https://www.ncbi.nlm.nih.gov/PUBMED/9990013).
- 886 **Vedovato N**, Ashcroft FM, Puljung MC. The Nucleotide-Binding Sites of SUR1: A Mechanistic
887 Model. *Biophys J*. 2015; 109(12):2452–60. [HTTPS://WWW.NCBI.NLM.NIH.GOV/PUBMED/26682803](https://www.ncbi.nlm.nih.gov/PUBMED/26682803),
888 doi: 10.1016/j.bpj.2015.10.026.
- 889 **Vehtari A**, Gelman A, Gabry J. Practical Bayesian model evaluation using leave-one-out cross-
890 validation and WAIC (vol 27, pg 1413, 2017). *Statistics and Computing*. 2017; 27(5):1433–1433.
891 <GotoISI>://WOS:000400831700018, doi: 10.1007/s11222-016-9709-3.
- 892 **Wagenmakers EJ**. A practical solution to the pervasive problems of p values. *Psychon Bull Rev*.
893 2007; 14(5):779–804. [HTTPS://WWW.NCBI.NLM.NIH.GOV/PUBMED/18087943](https://www.ncbi.nlm.nih.gov/PUBMED/18087943).
- 894 **Wang R**, Zhang X, Cui N, Wu J, Piao H, Wang X, Su J, Jiang C. Subunit-stoichiometric
895 evidence for kir6.2 channel gating, ATP binding, and binding-gating coupling. *Mol
896 Pharmacol*. 2007; 71(6):1646–56. [HTTPS://WWW.NCBI.NLM.NIH.GOV/PUBMED/17369308](https://www.ncbi.nlm.nih.gov/PUBMED/17369308), doi:
897 10.1124/mol.106.030528.
- 898 **Wu S**, Vysotskaya ZV, Xu X, Xie C, Liu Q, Zhou L. State-dependent cAMP binding to functioning
899 HCN channels studied by patch-clamp fluorometry. *Biophys J*. 2011; 100(5):1226–32. [HTTPS://WWW.NCBI.NLM.NIH.GOV/PUBMED/21354395](https://www.ncbi.nlm.nih.gov/PUBMED/21354395), doi: 10.1016/j.bpj.2011.01.034.
- 900
- 901 **Yan FF**, Lin YW, MacMullen C, Ganguly A, Stanley CA, Shyng SL. Congenital hyperinsulinism asso-
902 ciated ABCC8 mutations that cause defective trafficking of ATP-sensitive K⁺ channels: identifi-
903 cation and rescue. *Diabetes*. 2007; 56(9):2339–48. [HTTPS://WWW.NCBI.NLM.NIH.GOV/PUBMED/17575084](https://www.ncbi.nlm.nih.gov/PUBMED/17575084), doi: 10.2337/db07-0150.

- 905 Zagotta WN, Gordon MT, Senning EN, Munari MA, Gordon SE. Measuring distances between
906 TRPV1 and the plasma membrane using a noncanonical amino acid and transition metal ion
907 FRET. *J Gen Physiol.* 2016; 147(2):201–16. [HTTPS://WWW.NCBI.NLM.NIH.GOV/PUBMED/26755770](https://www.ncbi.nlm.nih.gov/pubmed/26755770),
908 doi: [10.1085/jgp.201511531](https://doi.org/10.1085/jgp.201511531).
- 909 Zerangue N, Schwappach B, Jan YN, Jan LY. A new ER trafficking signal regulates the subunit
910 stoichiometry of plasma membrane K(ATP) channels. *Neuron.* 1999; 22(3):537–48. [HTTPS://WWW.NCBI.NLM.NIH.GOV/PUBMED/10197533](https://www.ncbi.nlm.nih.gov/pubmed/10197533).
- 912 Zheng J, Zagotta WN. Patch-clamp fluorometry recording of conformational rearrangements of ion
913 channels. *Sci STKE.* 2003; 2003(176):PL7. [HTTPS://WWW.NCBI.NLM.NIH.GOV/PUBMED/12671191](https://www.ncbi.nlm.nih.gov/pubmed/12671191),
914 doi: [10.1126/stke.2003.176.pl7](https://doi.org/10.1126/stke.2003.176.pl7).

915 **Tables and supplementary figures**

Fluorescence Quenching	Construct	Term	Estimate	Standard Error
<i>TNP-ATP</i>	Kir6.2*-GFP+SUR1	EC_{50}	-4.59	0.05
	n = 18	h	0.82	0.05
		E_{max}	0.93	0.03
<i>Kir6.2*-G334D-GFP+SUR1</i>	Kir6.2*-G334D-GFP+SUR1	EC_{50}	-3.31	2.23
	n = 9	h	2.63	17.70
		E_{max}	0.08	0.26
<i>Kir6.2*-C166S-GFP+SUR1</i>	Kir6.2*-C166S-GFP+SUR1	EC_{50}	-4.50	0.05
	n = 12	h	0.92	0.08
		E_{max}	0.87	0.03
<i>Kir6.2*-GFP</i>	Kir6.2*-GFP	EC_{50}	-4.42	0.05
	n = 14	h	0.83	0.05
		E_{max}	0.92	0.03

Table 1. Table 1: Hill fit parameters from unroofed membranes. EC_{50} values and their standard errors are reported in $\log_{10} M^{-1}$.

Current Inhibition	Construct	Term	Estimate	Standard Error
<i>ATP</i>	Kir6.2-GFP+SUR1	IC_{50}	-4.20	0.07
	n = 3	h	1.28	0.21
		I_{max}	0.99	0.06
	Kir6.2-GFP	IC_{50}	-3.31	0.05
	n = 2	h	1.15	0.12
		I_{max}	0.93	0.03
	Kir6.2*-GFP+SUR1	IC_{50}	-4.10	0.06
	n = 4	h	1.42	0.21
		I_{max}	1.00	0.05
<i>TNP-ATP</i>	Kir6.2-GFP+SUR1	IC_{50}	-5.93	0.04
	n = 7	h	1.14	0.11
		I_{max}	0.97	0.02
	Kir6.2-GFP	IC_{50}	-3.56	0.64
	n = 3	h	1.09	0.85
		I_{max}	1.00	0.53
	Kir6.2*-GFP+SUR1	IC_{50}	-5.21	0.10
	n = 9	h	0.92	0.18
		I_{max}	0.96	0.05
	Kir6.2*-C166S-GFP+SUR1	IC_{50}	-2.71	51.05
	n = 6	h	1.14	15.79
		I_{max}	1.00	84.35
	Kir6.2*-GFP+SUR-K205A	IC_{50}	-3.78	0.45
	n = 9	h	0.75	0.30
		I_{max}	1.00	0.29
	Kir6.2*-GFP+SUR-K205E	IC_{50}	-3.20	2.15
	n = 9	h	0.79	0.84
		I_{max}	1.00	1.77
Fluorescence Quenching				
<i>TNP-ATP</i>	Kir6.2*-GFP+SUR1	EC_{50}	-4.11	0.09
	n = 9	h	0.87	0.11
		E_{max}	1.00	0.06
	Kir6.2*-C166S-GFP+SUR1	EC_{50}	-4.17	0.23
	n = 6	h	0.84	0.27
		E_{max}	1.00	0.14
	Kir6.2*-GFP+SUR-K205A	EC_{50}	-3.69	0.42
	n = 9	h	0.73	0.25
		E_{max}	1.00	0.27
	Kir6.2*-GFP+SUR-K205E	EC_{50}	-3.37	1.10
	n = 9	h	0.74	0.47
		E_{max}	1.00	0.79

Table 2. Table 2: Hill fit parameters from excised patches. EC_{50} values and their standard errors are reported in $\log_{10} M^{-1}$.

Full MWC Construct	Term	Estimate	2.5% Quantile	97.5% Quantile
Kir6.2*-GFP+SUR1 n = 9	L	-1.05	-1.85	-0.45
	D	0.04	0.00	0.19
	K_A	4.32	4.21	4.44
Kir6.2*-C166S-GFP+SUR1 n = 6	L	0.29	-1.04	1.41
	D	0.84	0.52	0.95
	K_A	4.18	3.93	4.47
Kir6.2*-GFP+SUR-K205A n = 9	L	-0.37	-1.34	0.41
	D	0.55	0.39	0.65
	K_A	3.76	3.59	3.95
Kir6.2*-GFP+SUR-K205E n = 9	L	-0.18	-1.25	0.70
	D	0.62	0.42	0.74
	K_A	3.40	3.21	3.62
Single-site				
Kir6.2*-GFP+SUR1 n = 9	L	-1.06	-1.84	-0.47
	D	0.05	0.01	0.10
	K_A	4.33	4.22	4.44
Kir6.2*-C166S-GFP+SUR1 n = 6	L	0.09	-1.15	1.05
	D	0.70	0.29	0.91
	K_A	4.15	3.88	4.43
Kir6.2*-GFP+SUR-K205A n = 9	L	-0.25	-1.30	0.53
	D	0.18	0.06	0.32
	K_A	3.62	3.45	3.83
Kir6.2*-GFP+SUR-K205E n = 9	L	-0.19	-1.19	0.52
	D	0.30	0.13	0.47
	K_A	3.31	3.13	3.50
Negative cooperativity				
Kir6.2*-GFP+SUR1 n = 9	L	-0.42	-1.38	0.48
	D	0.15	0.02	0.29
	K_A	4.82	4.54	5.29
	C	0.17	0.06	0.36
Kir6.2*-C166S-GFP+SUR1 n = 6	L	0.32	-0.96	1.47
	D	0.83	0.50	0.94
	K_A	4.43	4.04	5.14
	C	0.52	0.09	0.97
Kir6.2*-GFP+SUR-K205A n = 9	L	-0.16	-1.18	0.64
	D	0.52	0.32	0.64
	K_A	4.10	3.73	4.68
	C	0.35	0.10	0.91
Kir6.2*-GFP+SUR-K205E n = 9	L	0.03	-1.11	0.99
	D	0.58	0.32	0.73
	K_A	3.71	3.34	4.41
	C	0.45	0.10	0.96

Table 3. Table 3: Fitted parameters for the MWC-type models. L , K_A and their associated quantiles are reported as \log_{10} values to maintain consistency of the accuracy they are reported at.

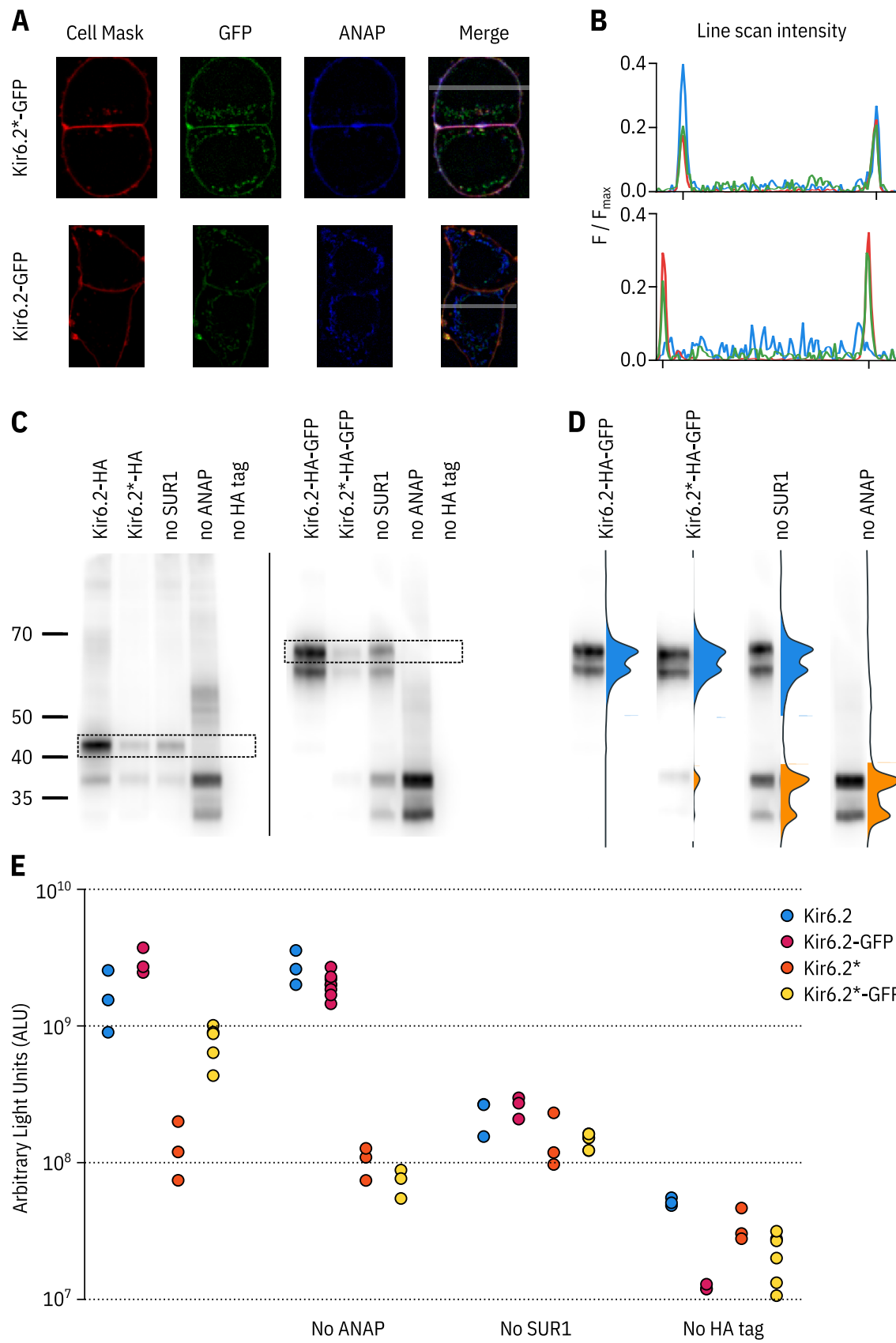


Figure 1 – figure supplement 1. ANAP labelling is specific and only full-length Kir6.2 is expressed at the cell membrane.

Figure 1 – figure supplement 1. ANAP labelling is specific and only full-length Kir6.2 is expressed at the cell membrane.

A. Confocal images of HEK-293T cells transfected with Kir6.2*-GFP + SUR1 (top panel) or Kir6.2-GFP + SUR1 (bottom panel). Cells were stained with Cell Mask Deep Red to label the plasma membrane. The grey band in the merged image is a 5-pixel width line scan. **B.** Averaged intensities of the line scans shown in **A**. The intensity of each channel is shown as a differently coloured line: Cell Mask in red, ANAP in blue and GFP in green. The notches on the x-axis mark the location of the plasma membrane. **C.** Two separate western blots against Kir6.2*-HA (left) and Kir6.2*-HA-GFP (right) constructs. Cells were co-transfected with pANAP, eRF1-E55D, and SUR1 unless otherwise indicated. Full-length Kir6.2 constructs are indicated on each gel with a dashed box. **D.** Each lane from the Kir6.2*-HA-GFP gel is displayed normalised to its highest intensity accompanied by the line averaged density trace. The density peak corresponding to ANAP-labelled Kir6.2 is filled in blue. The density peak for C-terminally truncated Kir6.2 is filled in orange. **E.** Chemiluminescence-based surface expression assay for Kir6.2-HA constructs. Each data point represents an individual coverslip of transfected HEK-293T cells. n = 3-6 for each condition. Note the logarithmic scale on the vertical axis.

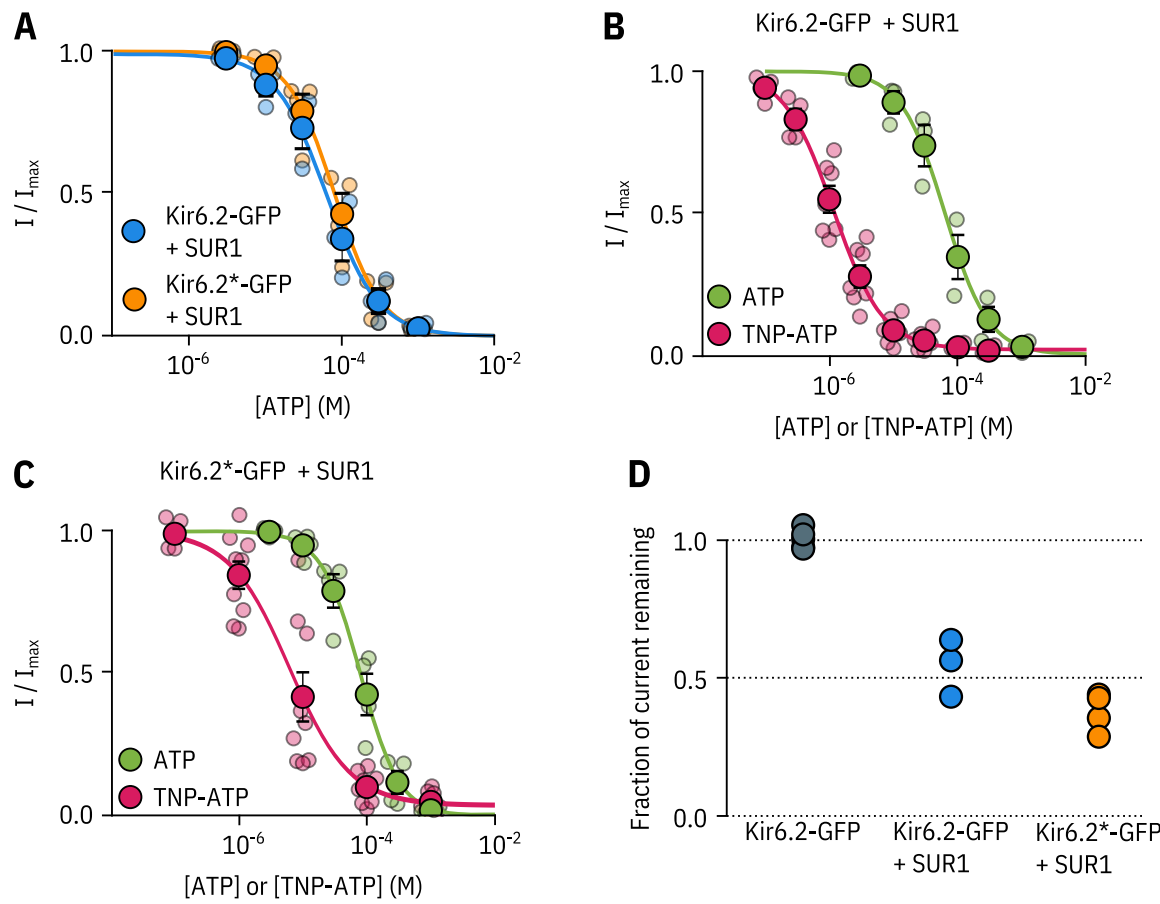


Figure 1 – figure supplement 2. Kir6.2*-GFP is functionally similar to Kir6.2-GFP. A. Concentration-response curve for ATP inhibition of Kir6.2-GFP + SUR1 or Kir6.2*-GFP + SUR1, measured in excised, inside-out patches. The smooth curves are descriptive Hill fits to the data. Kir6.2-GFP + SUR1: $IC_{50} = 62.7 \mu\text{M}$, $h = 1.28$, $I_{max} = 0.99$, $n = 3$; Kir6.2*-GFP + SUR1: $IC_{50} = 79.5 \mu\text{M}$, $h = 1.42$, $I_{max} = 1.00$, $n = 4$. **B, C.** Concentration-response relationships for current inhibition in excised, inside-out patches expressing Kir6.2-GFP + SUR1 (**C**) or Kir6.2*-GFP + SUR1 (**D**) exposed to either ATP or TNP-ATP. The smooth curves are descriptive Hill fits to the data. Kir6.2-GFP + SUR1 (TNP-ATP): $IC_{50} = 1.17 \mu\text{M}$, $h = 1.14$, $I_{max} = 0.97$, $n = 7$, Kir6.2*-GFP + SUR1 (TNP-ATP): $IC_{50} = 6.23 \mu\text{M}$, $h = 0.92$, $I_{max} = 0.96$, $n = 9$. Data and fits for inhibition of Kir6.2*-GFP + SUR1 by TNP-ATP are the same as in Figure 2. **D.** Fractional current inhibition by 100 μM tolbutamide measured in excised, inside-out patches. Data were normalised to the average current in control solution before and after tolbutamide exposure. Each data point represents an individual patch. Kir6.2-GFP without SUR1, $n = 5$; Kir6.2-GFP + SUR1, $n = 3$; Kir6.2*-GFP + SUR1, $n = 4$.

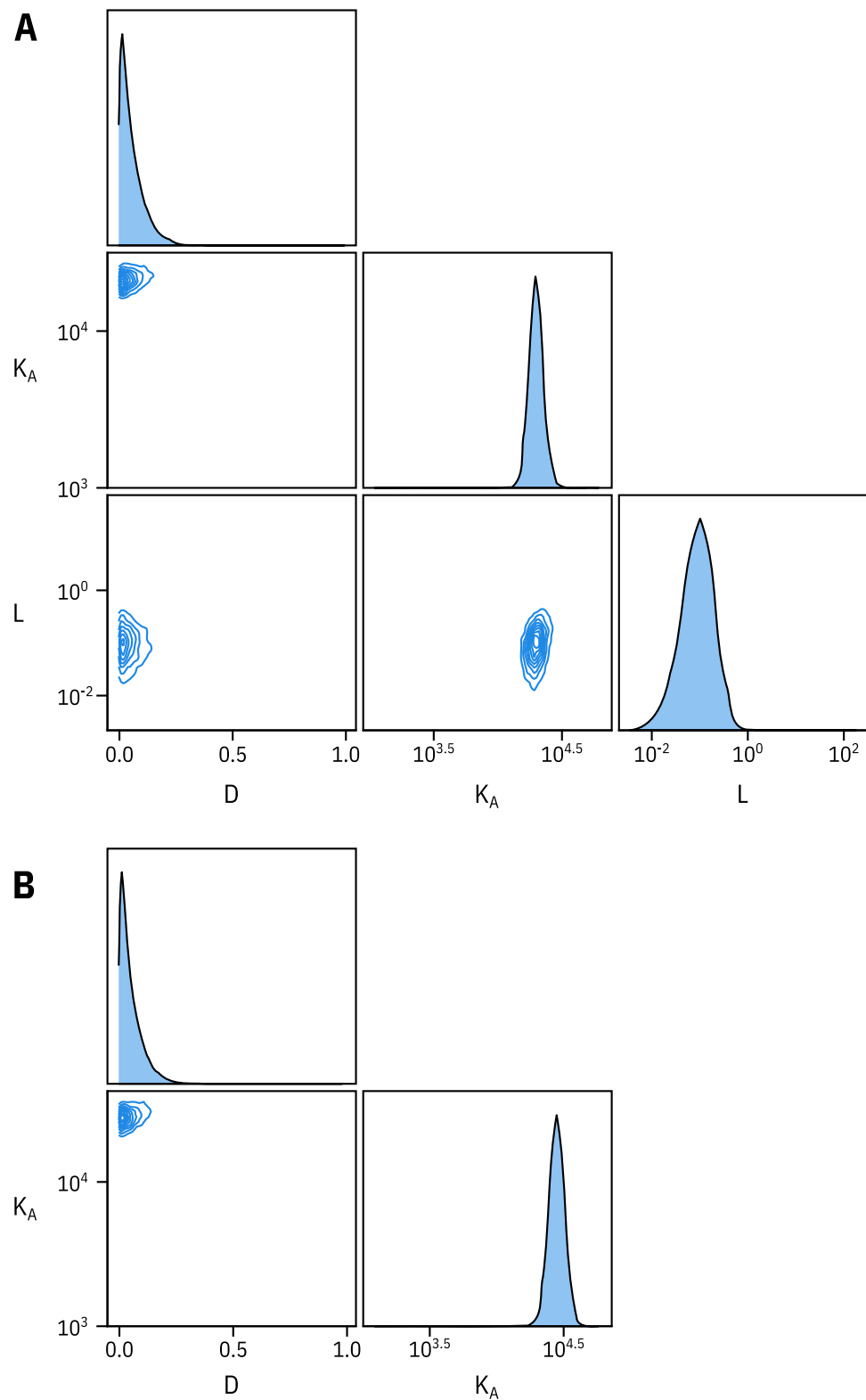


Figure 2 – figure supplement 1. Fixing L does not affect estimates of D and K_A . **A.** Pairwise correlation plots of L , D and K_A from the full MWC-type model fit to Kir6.2*-GFP + SUR1. **B.** Pairwise correlation plots of D and K_A from the full MWC-type with L fixed to 0.8 ($P_{open} = 0.45$).

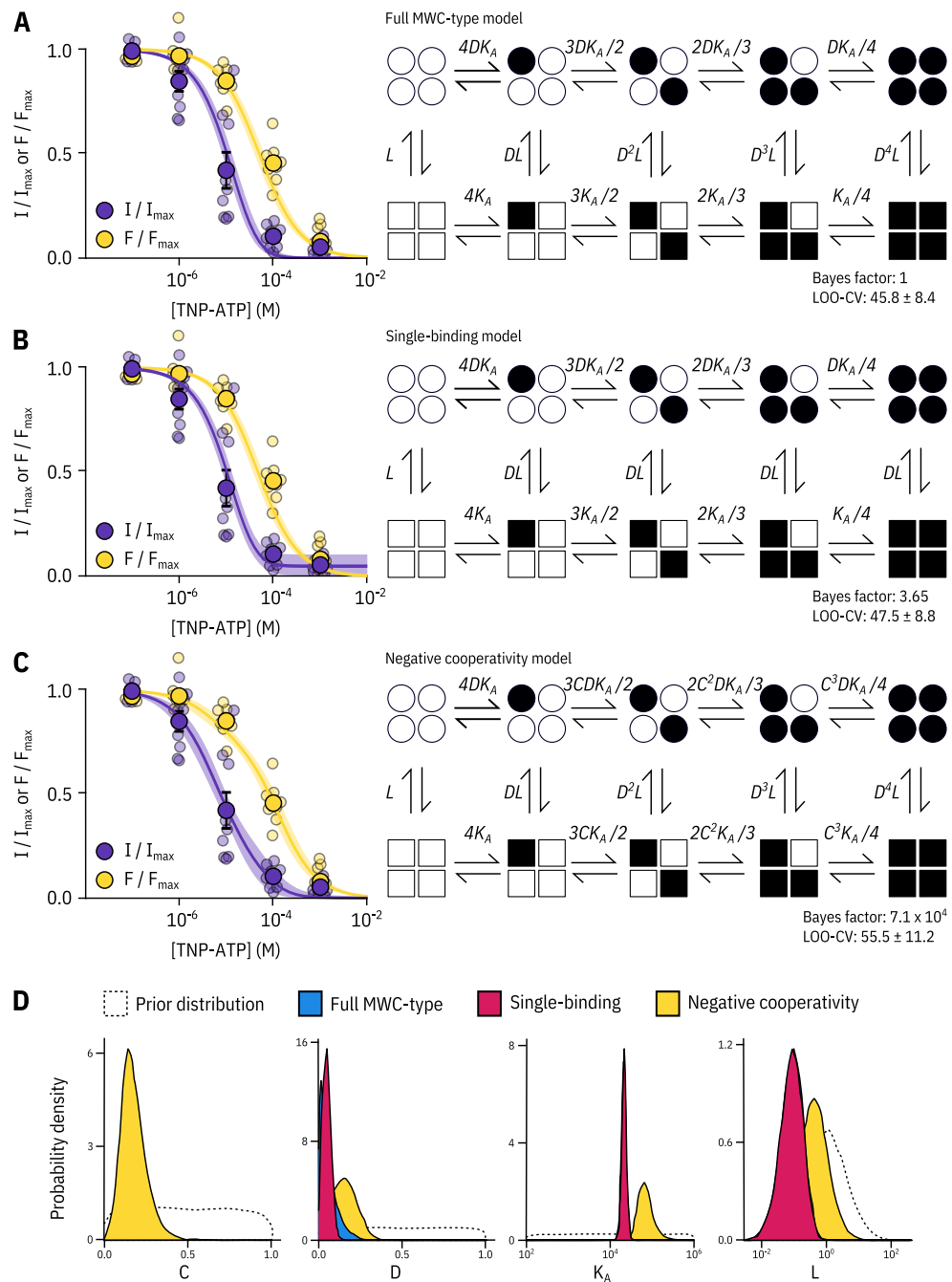


Figure 2 – figure supplement 2. Model selection. Fits to PCF data from Figure 2 with the full MWC-type model (**A**), single-binding model (**B**) and negative-cooperativity model (**C**) are shown on the left with the diagrammatic formulation of each model on the right. The Bayes factor and leave-one-out cross-validation (LOO-CV) scores for each model compared to the full MWC-type model are displayed. L , D , C , and K_A are defined in the text. **D**. Posterior probability distributions for the each of the models generated by MCMC fits to the data in Figure 2 overlaid on the prior probability distribution (dashed line) for each parameter. For L and K_A , the distributions for the MWC-type and single-binding model were virtually identical. The MWC-type densities are hidden behind the single-binding densities.

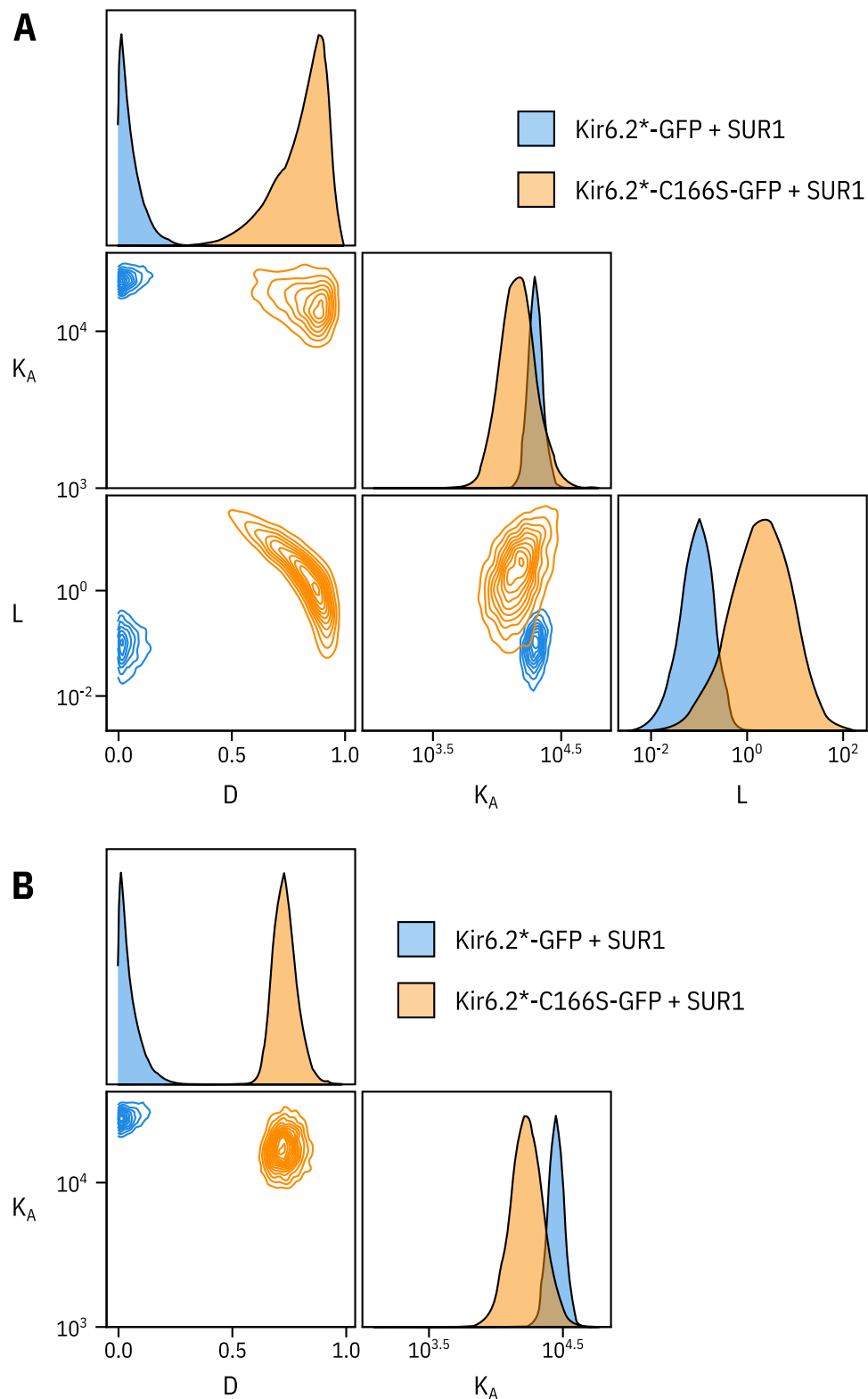


Figure 3 – figure supplement 1. Fixing L does not affect the other two parameters. **A.** Pairwise correlation plots of L , D and K_A from the full MWC-type model fit to $\text{Kir}6.2^*\text{-GFP} + \text{SUR1}$ and $\text{Kir}6.2^*\text{-C166S-GFP} + \text{SUR1}$. **B.** Pairwise correlation plots of D and K_A from the full MWC-type with L fixed to 0.8 for $\text{Kir}6.2^*\text{-GFP} + \text{SUR1}$ ($P_{open} = 0.45$) or 6.0 for $\text{Kir}6.2^*\text{-C166S-GFP} + \text{SUR1}$ ($P_{open} = 0.86$).

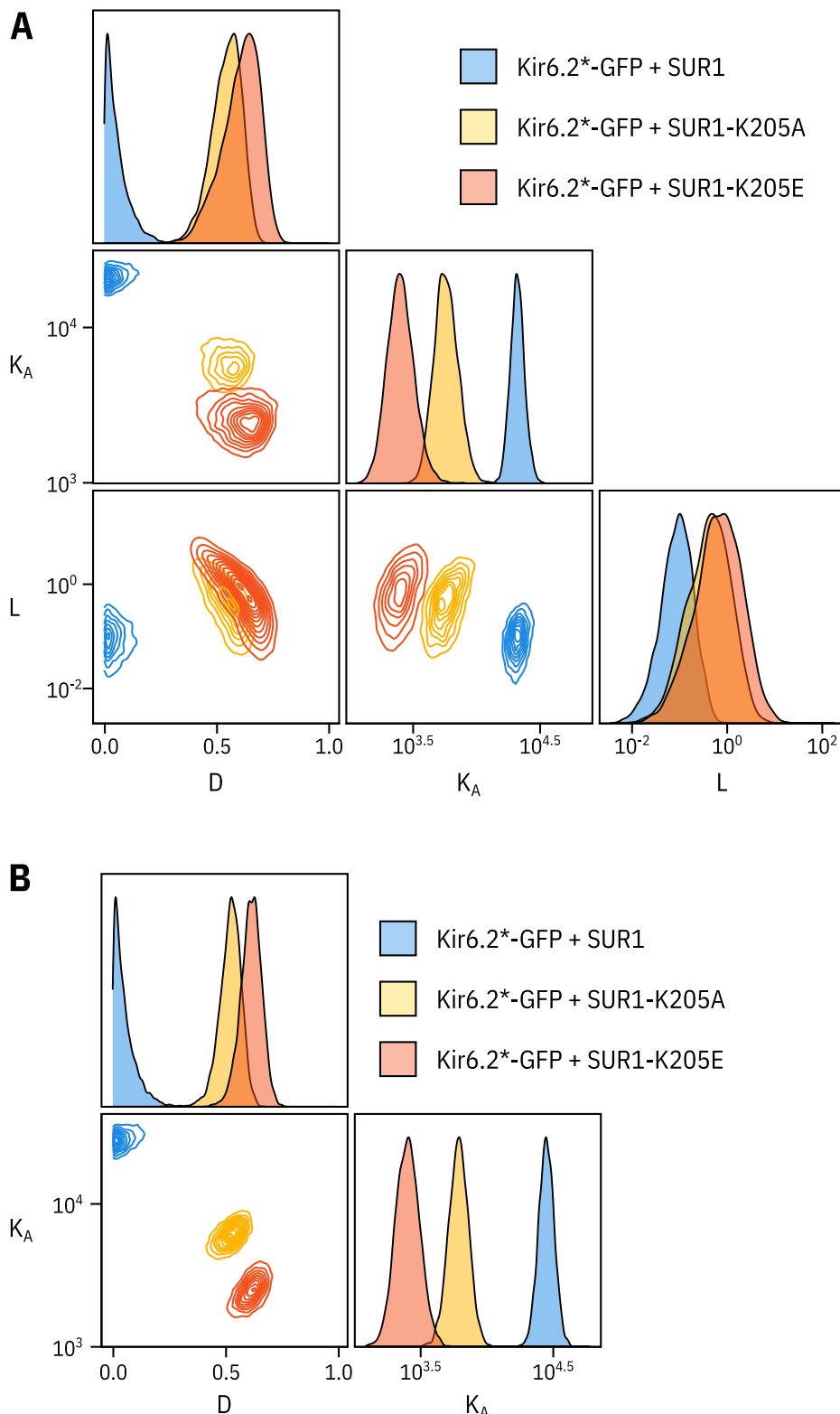


Figure 5 – figure supplement 1. Fixing the L parameter does not drastically affect the fits to the SUR1-K205A or

SUR1-K205E data. A. Pairwise correlation plots of L , D and K_A from the full MWC-type model fit to Kir6.2*-GFP co-expressed with wild-type SUR1, SUR1-K205A, and SUR1-K205E. **B.** Pairwise correlation plots of D and K_A from the full MWC-type as above with L fixed to 0.8 (*Trapp et al., 1998*).

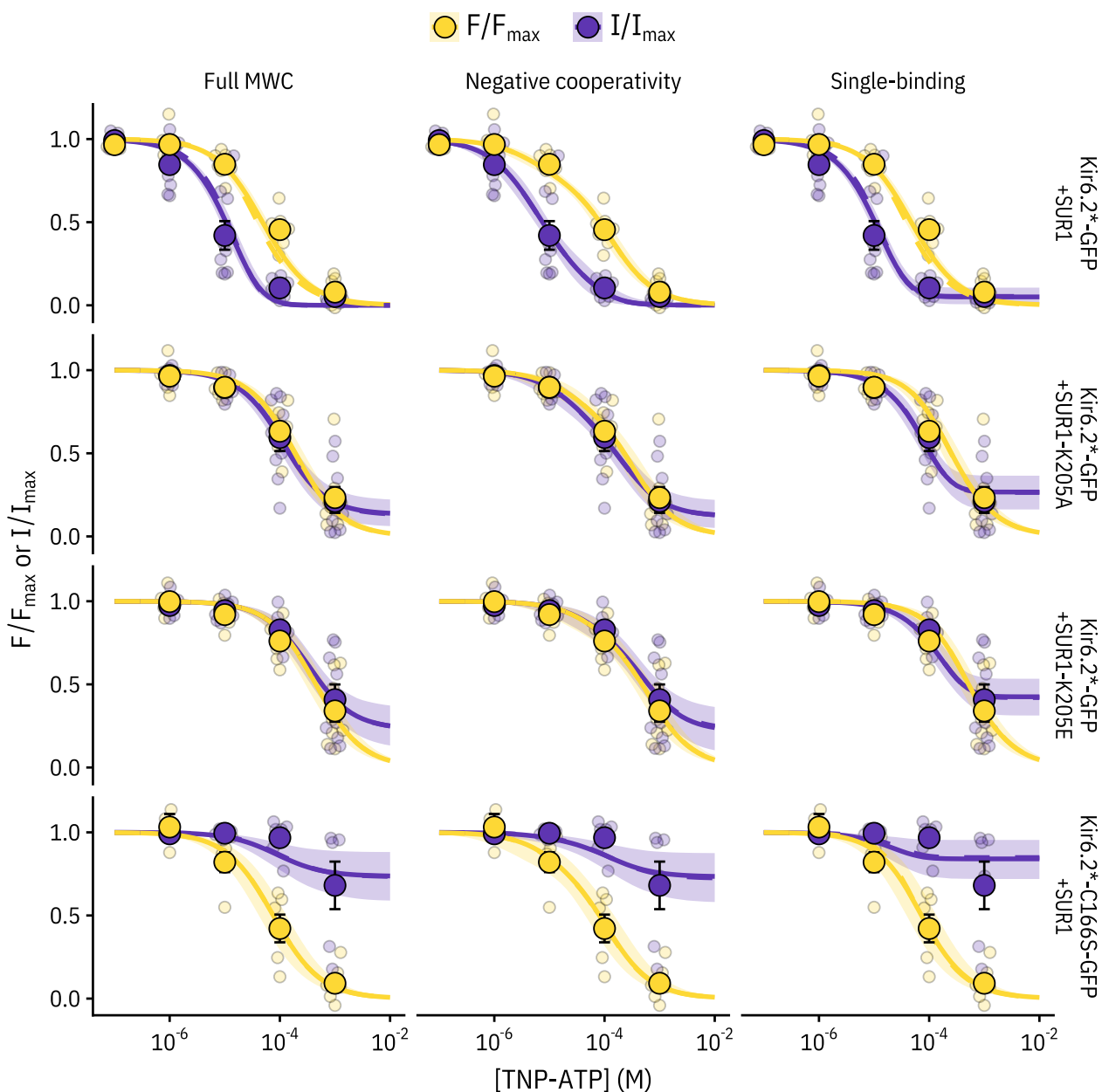
A

Figure 5 – figure supplement 1. Comparing the ability of each model to explain the data. Fits for each construct with each model (MWC-type, single-binding, negative-cooperativity) are displayed with the solid curve representing the median fit, the shaded area representing the 95% quartiles, and the dashed curve representing the median fit if the L parameter is fixed (to 6.0 for Kir6.2*-C166S-GFP + SUR1 and to 0.8 for the other three constructs). As the two fits were very similar, the dashed curve mostly overlays the solid curve. The most notable differences between the fits are that the negative cooperativity model allows for non-sigmoidal curves, and the single-binding model predicts much larger pedestals of current at saturating concentrations of TNP-ATP than either of the other two models.